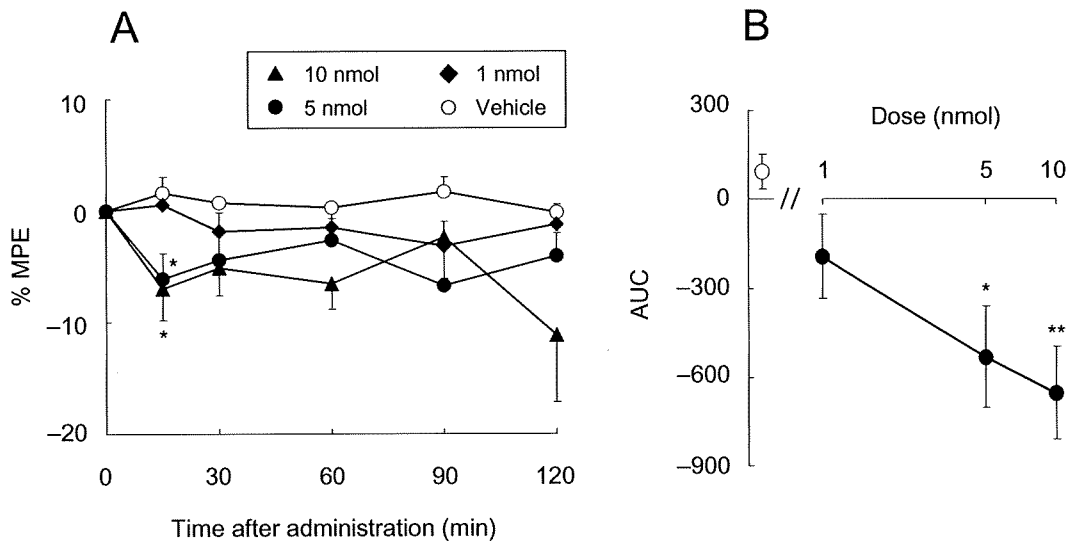

Figure 5 (A) Effect of mecamylamine injected intra-VPL on neuropathic tactile allodynia. Data are presented as a percentage of the maximum possible effect (% MPE). Each point represents the mean ± SEM of the ligated paws of five to six animals per group. *$P < 0.05$ versus vehicle at the same time point. (B) Dose-response curve of mecamylamine-induced hyperalgesia. The open symbol represents the AUC of the vehicle-treated group, and the closed symbols represent that of each concentration of the mecamylamine-treated group. *$P < 0.05$, **$P < 0.01$ versus vehicle. AUC, area under the curves; MPE, maximal possible effect; VPL, ventral posterolateral thalamic nucleus.

nACh receptor activation, we evaluated the effect of intra-VPL administered mecamylamine on the anti-allodynic effects produced by i.c.v. administered 5IA. The results from the ligated paws are illustrated in Figure 4C. Two-way ANOVA demonstrated significant main effects of treatment ($F_{3,105} = 7.91$, $P = 0.001$) and time ($F_{4,105} = 5.65$, $P < 0.001$) and a significant interaction between treatment and time ($F_{12,105} = 2.49$, $P = 0.008$). The rats administered vehicle intra-VPL followed by 10 nmol of 5IA i.c.v. (Vehicle/5IA group) demonstrated significantly elevated % MPE values at 15 and 30 min after administration. This result was consistent with the anti-allodynic effect produced by i.c.v. administered 5IA (Figure 1). Pretreatment with intra-VPL mecamylamine (10 nmol) significantly inhibited the effect of i.c.v. administered 5IA (10 nmol). The % MPE values for rats treated with mecamylamine alone (MEC/Vehicle group) also tended to decrease compared with those of the vehicle treated rats, although the difference was not significant.

Hyperalgesic effect of intra-VPL administered mecamylamine

To examine the effects of mecamylamine on tactile allodynia in more detail, we injected multiple doses of mecamylamine intra-VPL and performed the von Frey filament test. Data from the ligated paws are shown in Figure 5A. There was a significant main effect of treatment ($F_{3,95} = 6.77$, $P = 0.003$) but no effect of time nor interaction between time and treatment. The *post hoc* Tukey test demonstrated a significant difference between vehicle-treated group and 5 nmol- or 10 nmol-treated groups. The calculated area under the curves of each group clearly demonstrated the dose-dependent hyperalgesic effects of mecamylamine (Figure 5B).

Effects of 5IA and mecamylamine on motor function

We conducted an inclined plane test to evaluate the effects of 5IA and mecamylamine on general motor functions. The maximum angle that the rats were able to endure before slipping down the plane was not significantly different between the vehicle and drug-treated groups at any time point (Table 1, data not shown for mecamylamine).

Table 1 Effects of 5IA on motor functions

Drug	*Time after administration*				
	15 min	*30 min*	*60 min*	*90 min*	*120 min*
i.c.v.					
Vehicle	98 ± 1	102 ± 4	98 ± 2	92 ± 3	94 ± 3
5IA	93 ± 2	97 ± 3	88 ± 4	96 ± 3	93 ± 1
Intra-VPL					
Vehicle	99 ± 3	99 ± 2	97 ± 4	100 ± 2	97 ± 3
5IA	100 ± 4	97 ± 2	99 ± 2	97 ± 1	102 ± 2

Data are expressed as a percentage of the control level ('angle of sliding'), which was determined before drug administration in each animal, and represent the mean ± SEM of five to six animals per group. No significant difference was observed between the two groups (two-way ANOVA with repeated measures).
5IA, 5-iodo-3-(2(S)-azetidinylmethoxy)pyridine; VPL, ventral posterolateral thalamic nucleus.

Discussion and Conclusions

In the present study, we examined the changes in central nACh receptor density in a rat model of neuropathic pain and the involvement of nACh receptors in anti-nociceptive effects in the region where changes occurred. First, we evaluated the anti-allodynic effect of 5IA after i.c.v. administration and found that the anti-allodynic effect was dose-dependent. Because the effect was completely antagonized by mecamylamine, the anti-allodynic effect of 5IA must occur via nACh receptors. No significant difference was observed between the

vehicle and 5IA treated groups in the inclined plane test suggesting that 5IA exhibited anti-allodynic effects without affecting motor functions.

We found that bilateral up-regulation of thalamic nACh receptors occurred in the PSL model of neuropathic pain. This is the first report of up-regulation of thalamic nACh receptors under chronic painful conditions. Because the up-regulation of both muscarinic and cannabinoid CB_1 receptors have been reported to contribute to the increased analgesic efficacy of each agonist (Siegling *et al.*, 2001; Chen and Pan, 2003), up-regulated nACh receptors may also contribute to the potentiation of anti-allodynic effects produced by nACh receptor agonists and attenuate neuropathic pain. Consistent with Seltzer's report (Seltzer *et al.*, 1990), the unilateral PSL caused bilateral tactile allodynia in the present study; and thus, the up-regulation must occur bilaterally. In the present study, we performed an autoradiographic saturation assay to determine the regional B_{max} of nACh receptors. As no report concerning autoradiographic saturation assays using [^{125}I]5IA has been published, it is important to validate the method used. Doura *et al.* (2008) performed quantitative autoradiography using [^{125}I]5IA, but, in their study, they incubated brain slices with only a single concentration of [^{125}I]5IA and did not perform a saturation assay. Thus, a direct comparison between our present data and theirs is not possible. Nevertheless, the ratios of the thalamus to the striatum or the cortex of our present data were consistent in the data reported by Doura *et al.* (2008), suggesting that our method was valid.

A previous PET study showed that the increase in cerebral blood flow in the VPL positively correlated with pain intensity, suggesting involvement of the VPL in pain transmission (Derbyshire *et al.*, 1997). Furthermore, electrical stimulation of the VPL has produced pain alleviation in both rat models and patients with neuropathic pain (Kupers and Gybels, 1993; Gybels, 2001). These findings suggest that the VPL is involved in the expression of anti-nociceptive effects. Indeed, we demonstrated that 5IA administered locally into the VPL significantly and dose-dependently reversed tactile allodynia. This effect was antagonized by coadministered mecamylamine. As no significant difference was observed between the vehicle and 5IA treated groups in the results of an inclined plane test, the changes in % MPE values observed in the 5IA treated groups were considered to reflect the analgesic effect, not motor dysfunction. These findings suggest that the nACh receptors expressed in the VPL were involved in the anti-allodynic effect that occurred after nACh receptor agonist administration. This was consistent with the finding that blockade of nACh receptors in the VPL caused a decrease in the anti-allodynic effect of i.c.v.-administered 5IA. Moreover, the intra-VPL injection of mecamylamine alone induced significant decreases in % MPE values. Mecamylamine is not an inverse agonist, but a non-competitive antagonist (Jensen *et al.*, 2005). Thus, during neuropathic pain, an intrinsic anti-allodynic mechanism by which ACh activates nACh receptors expressed in the VPL may be present and antagonism of these receptors by mecamylamine causes the hyperalgesic effect. That is to say, the nACh receptors expressed in the VPL may participate in anti-allodynic effects produced not only by exogenous but also endogenous agonists.

The present findings do not negate the involvement of nACh receptors in anti-allodynic effects outside of the VPL. Previous pharmacological studies reported that the central sites involved in nACh receptor-mediated antinociception were the NRM and the PPTg. The antinociception produced by nicotinic stimulation of the PPTg or the NRM depended upon muscarinic cholinergic, 5-hydroxytryptaminergic and adrenergic systems at the level of the lumbar spinal cord (Iwamoto and Marion, 1993). Curzon *et al.* (1998) showed that microinjection of nACh receptor agonists (epibatidine and A-85380) into the NRM produced antinociception against heat stimuli, and these effects were prevented by coadministration of mecamylamine into the NRM. Indeed, we demonstrated that VPL blockade by mecamylamine before i.c.v. administration of 5IA decreased the anti-allodynic effect by up to approximately 70%, not 100%. Thus, the remainder of the anti-allodynic effect is possibly caused by the binding of 5IA to the NRM and/or the PPTg.

Recently, Mogg *et al.* (2004) have reported that 5IA can functionally activate the α4β2-nACh and α6β2-nACh receptors. However, Perry *et al.* have reported that the nACh receptors expressed in the thalamus are mainly of the α4β2 sub-type (Perry *et al.*, 2002) and that the α6 subunit is present in less than 4% of the thalamic nACh receptors (Perry *et al.*, 2007). Therefore, the anti-allodynic effect we reported was probably mediated via the α4β2-nACh receptors, at least when 5IA was administered into the VPL. Whereas many results have shown that α4 subunit-containing nACh receptors play an important role in nACh receptor-mediated antinociception (Bitner *et al.*, 1998; Marubio *et al.*, 1999; Bitner *et al.*, 2000), the contribution of the α6β2-nACh receptors to the anti-nociceptive effect is unknown. As A-186253 has been developed as a specific antagonist of the α4β2-nACh receptors (Itier *et al.*, 2004), it may be possible to investigate α6β2-nACh receptor-mediated antinociception using both 5IA and A-186253.

In summary, we have demonstrated for the first time that up-regulation of thalamic nACh receptors occurs in a model of chronic pain. Moreover, we found that intra-VPL administration of 5IA attenuated tactile allodynia, dose-dependently. This effect was completely antagonized by co-administered mecamylamine. The blockade of nACh receptors in the VPL by mecamylamine caused a decrease in the anti-allodynic effect of i.c.v.-administered 5IA. These findings indicate that the nACh receptors expressed in the VPL are a potential site of the anti-nociceptive action produced by 5IA. Furthermore, mecamylamine, given intra-VPL, induced a hyperalgesic effect. This effect is likely to be responsible for the mecamylamine antagonism of the intrinsic anti-allodynic mechanism induced by endogenous acetylcholine. These findings suggest that the nACh receptors expressed in the VPL play an important role in the anti-allodynic effects produced by exogenous and endogenous agonists.

Acknowledgements

We thank Dr Takayuki Nakagawa (Department of Molecular Pharmacology, Graduate School of Pharmaceutical Sciences, Kyoto University) for his technical support and invaluable discussion regarding the behavioural tests. This work was

supported in part by a Grant-in-Aid for Scientific Research (A) (19209041) and a Grant-in-Aid for Young Scientists (B) (19790869) from the Ministry of Education, Culture, Sports, Science and Technology of Japan, and a grant from the Smoking Research Foundation.

Conflicts of interest

The authors state that they have no conflicts of interest.

References

Alexander SPH, Mathie A, Peters JA (2008). Guide to Receptors and Channels (GRAC), 3rd edn. *Br J Pharmacol* **153** (Suppl. 2): S1–S209.

Bannon AW, Decker MW, Curzon P, Buckley MJ, Kim DJ, Radek RJ *et al.* (1998a). ABT-594 [(R)-5-(2-azetidinylmethoxy)-2-chloropyridine]: a novel, orally effective antinociceptive agent acting via neuronal nicotinic acetylcholine receptors: II. In vivo characterization. *J Pharmacol Exp Ther* **285**: 787–794.

Bannon AW, Decker MW, Holladay MW, Curzon P, Donnelly-Roberts D, Puttfarcken PS *et al.* (1998b). Broad-spectrum, non-opioid analgesic activity by selective modulation of neuronal nicotinic acetylcholine receptors. *Science* **279**: 77–81.

Bannon AW, Decker MW, Kim DJ, Campbell JE, Arneric SP (1998c). ABT-594, a novel cholinergic channel modulator, is efficacious in nerve ligation and diabetic neuropathy models of neuropathic pain. *Brain Res* **801**: 158–163.

Bitner RS, Nikkel AL, Curzon P, Arneric SP, Bannon AW, Decker MW (1998). Role of the nucleus raphe magnus in antinociception produced by ABT-594: immediate early gene responses possibly linked to neuronal nicotinic acetylcholine receptors on serotonergic neurons. *J Neurosci* **18**: 5426–5432.

Bitner RS, Nikkel AL, Curzon P, Donnelly-Roberts DL, Puttfarcken PS, Namovic M *et al.* (2000). Reduced nicotinic receptor-mediated antinociception following in vivo antisense knock-down in rat. *Brain Res* **871**: 66–74.

Brasic JR, Zhou Y, Musachio JL, Hilton J, Fan H, Crabb A *et al.* (2009). Single photon emission computed tomography experience with (S)-5-[(123)I]iodo-3-(2-azetidinylmethoxy)pyridine in the living human brain of smokers and nonsmokers. *Synapse* **63**: 339–358.

Chen SR, Pan HL (2003). Up-regulation of spinal muscarinic receptors and increased antinociceptive effect of intrathecal muscarine in diabetic rats. *J Pharmacol Exp Ther* **307**: 676–681.

Curzon P, Nikkel AL, Bannon AW, Arneric SP, Decker MW (1998). Differences between the antinociceptive effects of the cholinergic channel activators A-85380 and (+/−)-epibatidine in rats. *J Pharmacol Exp Ther* **287**: 847–853.

Decker MW, Curzon P, Holladay MW, Nikkel AL, Bitner RS, Bannon AW *et al.* (1998). The role of neuronal nicotinic acetylcholine receptors in antinociception: effects of ABT-594. *J Physiol Paris* **92**: 221–224.

Decker MW, Rueter LE, Bitner RS (2004). Nicotinic acetylcholine receptor agonists: a potential new class of analgesics. *Curr Top Med Chem* **4**: 369–384.

Derbyshire SW, Jones AK, Gyulai F, Clark S, Townsend D, Firestone LL (1997). Pain processing during three levels of noxious stimulation produces differential patterns of central activity. *Pain* **73**: 431–445.

Donnelly-Roberts DL, Puttfarcken PS, Kuntzweiler TA, Briggs CA, Anderson DJ, Campbell JE *et al.* (1998). ABT-594 [(R)-5-(2-azetidinylmethoxy)-2-chloropyridine]: a novel, orally effective analgesic acting via neuronal nicotinic acetylcholine receptors: I. In vitro characterization. *J Pharmacol Exp Ther* **285**: 777–786.

Doura MB, Gold AB, Keller AB, Perry DC (2008). Adult and periadolescent rats differ in expression of nicotinic cholinergic receptor subtypes and in the response of these subtypes to chronic nicotine exposure. *Brain Res* **1215**: 40–52.

Fukui M, Nakagawa T, Minami M, Satoh M (2001). Antinociceptive effects of intracerebroventricularly administered P2 purinoceptor agonists in the rat. *Eur J Pharmacol* **419**: 25–31.

Gybels J (2001). Thalamic stimulation in neuropathic pain: 27 years later. *Acta Neurol Belg* **101**: 65–71.

Holladay MW, Wasicak JT, Lin NH, He Y, Ryther KB, Bannon AW *et al.* (1998). Identification and initial structure-activity relationships of (R)-5-(2-azetidinylmethoxy)-2-chloropyridine (ABT-594), a potent, orally active, non-opiate analgesic agent acting via neuronal nicotinic acetylcholine receptors. *J Med Chem* **41**: 407–412.

Itier V, Schonbachler R, Tribollet E, Honer M, Prinz K, Marguerat A *et al.* (2004). A-186253, a specific antagonist of the alpha 4 beta 2 nAChRs: its properties and potential to study brain nicotinic acetylcholine receptors. *Neuropharmacology* **47**: 538–557.

Iwamoto ET, Marion L (1993). Adrenergic, serotonergic and cholinergic components of nicotinic antinociception in rats. *J Pharmacol Exp Ther* **265**: 777–789.

Jain KK (2004). Modulators of nicotinic acetylcholine receptors as analgesics. *Curr Opin Investig Drugs* **5**: 76–81.

Jensen AA, Frolund B, Liljefors T, Krogsgaard-Larsen P (2005). Neuronal nicotinic acetylcholine receptors: structural revelations, target identifications, and therapeutic inspirations. *J Med Chem* **48**: 4705–4745.

Kanegawa N, Kiyono Y, Kimura H, Sugita T, Kajiyama S, Kawashima H *et al.* (2006). Synthesis and evaluation of radioiodinated (S,S)-2-(alpha-(2-iodophenoxy)benzyl)morpholine for imaging brain norepinephrine transporter. *Eur J Nucl Med Mol Imaging* **33**: 639–647.

Kupers RC, Gybels JM (1993). Electrical stimulation of the ventroposterolateral thalamic nucleus (VPL) reduces mechanical allodynia in a rat model of neuropathic pain. *Neurosci Lett* **150**: 95–98.

Mamede M, Ishizu K, Ueda M, Mukai T, Iida Y, Fukuyama H *et al.* (2004). Quantification of human nicotinic acetylcholine receptors with ^{123}I-5IA SPECT. *J Nucl Med* **45**: 1458–1470.

Mamede M, Ishizu K, Ueda M, Mukai T, Iida Y, Kawashima H *et al.* (2007). Temporal change in human nicotinic acetylcholine receptor after smoking cessation: 5IA SPECT study. *J Nucl Med* **48**: 1829–1835.

Marcil J, Walczak JS, Guindon J, Ngoc AH, Lu S, Beaulieu P (2006). Antinociceptive effects of tetrodotoxin (TTX) in rodents. *Br J Anaesth* **96**: 761–768.

Marubio LM, del Mar Arroyo-Jimenez M, Cordero-Erausquin M, Lena C, Le Novere N, de Kerchove d'Exaerde A *et al.* (1999). Reduced antinociception in mice lacking neuronal nicotinic receptor subunits. *Nature* **398**: 805–810.

Mogg AJ, Jones FA, Pullar IA, Sharples CG, Wonnacott S (2004). Functional responses and subunit composition of presynaptic nicotinic receptor subtypes explored using the novel agonist 5-iodo-A-85380. *Neuropharmacology* **47**: 848–859.

Mukhin AG, Gundisch D, Horti AG, Koren AO, Tamagnan G, Kimes AS *et al.* (2000). 5-Iodo-A-85380, an alpha4beta2 subtype-selective ligand for nicotinic acetylcholine receptors. *Mol Pharmacol* **57**: 642–669.

Oishi N, Hashikawa K, Yoshida H, Ishizu K, Ueda M, Kawashima H *et al.* (2007). Quantification of nicotinic acetylcholine receptors in Parkinson's disease with (123)I-5IA SPECT. *J Neurol Sci* **256**: 52–60.

Okada M, Nakagawa T, Minami M, Satoh M (2002). Analgesic effects of intrathecal administration of P2Y nucleotide receptor agonists UTP and UDP in normal and neuropathic pain model rats. *J Pharmacol Exp Ther* **303**: 66–73.

Paxinos G, Watson C (2005). *The Rat Brain in Stereotaxic Coordinates*, 5th edn. Elsevier Academic Press: San Diego, CA.

Perry DC, Xiao Y, Nguyen HN, Musachio JL, Davila-Garcia MI, Kellar KJ (2002). Measuring nicotinic receptors with characteristics of alpha4beta2, alpha3beta2 and alpha3beta4 subtypes in rat tissues by autoradiography. *J Neurochem* **82**: 468–481.

Perry DC, Mao D, Gold AB, McIntosh JM, Pezzullo JC, Kellar KJ (2007). Chronic nicotine differentially regulates alpha6- and beta3-containing nicotinic cholinergic receptors in rat brain. *J Pharmacol Exp Ther* **322**: 306–315.

Saji H, Ogawa M, Ueda M, Iida Y, Magata Y, Tominaga A *et al.* (2002). Evaluation of radioiodinated 5-iodo-3-(2(S)-azetidinylmethoxy) pyridine as a ligand for SPECT investigations of brain nicotinic acetylcholine receptors. *Ann Nucl Med* **16**: 189–200.

Seltzer Z, Dubner R, Shir Y (1990). A novel behavioral model of neuropathic pain disorders produced in rats by partial sciatic nerve injury. *Pain* **43**: 205–218.

Siegling A, Hofmann HA, Denzer D, Mauler F, De Vry J (2001). Cannabinoid CB(1) receptor upregulation in a rat model of chronic neuropathic pain. *Eur J Pharmacol* **415**: R5–R7.

Sindrup SH, Jensen TS (1999). Efficacy of pharmacological treatments of neuropathic pain: an update and effect related to mechanism of drug action. *Pain* **83**: 389–400.

Suzdak PD, Foged C, Andersen KE (1994). Quantitative autoradiographic characterization of the binding of [^{3}H]tiagabine (NNC 05-328) to the GABA uptake carrier. *Brain Res* **647**: 231–241.

Tanaka K, Fukuuchi Y, Gomi S, Takashima S, Mihara B, Shirai T *et al.* (1993). Reduction in second-messenger ligand binding sites after brain ischemia – autoradiographic Bmax and Kd determinations using digital image analysis. *Brain Res Bull* **32**: 49–56.

Ueda M, Iida Y, Kitamura Y, Kawashima H, Ogawa M, Magata Y *et al.* (2008). 5-Iodo-A-85380, a specific ligand for alpha4beta2 nicotinic acetylcholine receptors, prevents glutamate neurotoxicity in rat cortical cultured neurons. *Brain Res* **1199**: 46–52.

Ueda M, Iida Y, Mukai T, Mamede M, Ishizu K, Ogawa M *et al.* (2004). 5-[^{123}I]Iodo-A-85380: assessment of pharmacological safety, radiation dosimetry and SPECT imaging of brain nicotinic receptors in healthy human subjects. *Ann Nucl Med* **18**: 337–344.

Vaupel DB, Tella SR, Huso DL, Mukhin AG, Baum I, Wagner VO *et al.* (2003). Pharmacology, toxicology, and radiation dosimetry evaluation of [I-123]5-I-a-85380, a radioligand for in vivo imaging of cerebral neuronal nicotinic acetylcholine receptors in humans. *Drug Dev Res* **58**: 149–168.

Yasuda T, Miki S, Yoshinaga N, Senba E (2005). Effects of amitriptyline and gabapentin on bilateral hyperalgesia observed in an animal model of unilateral axotomy. *Pain* **115**: 161–170.

Imaging of HIF-1-Active Tumor Hypoxia Using a Protein Effectively Delivered to and Specifically Stabilized in HIF-1-Active Tumor Cells

Takashi Kudo[1], Masashi Ueda[1,2], Yuji Kuge[1], Takahiro Mukai[3], Shotaro Tanaka[4], Maki Masutani[1], Yasushi Kiyono[2,5], Shinae Kizaka-Kondoh[4], Masahiro Hiraoka[4], and Hideo Saji[1]

[1]Department of Patho-Functional Bioanalysis, Graduate School of Pharmaceutical Sciences, Kyoto University, Kyoto, Japan; [2]Radioisotopes Research Laboratory, Faculty of Medicine, Kyoto University Hospital, Kyoto University, Kyoto, Japan; [3]Department of Biomolecular Recognition Chemistry, Graduate School of Pharmaceutical Sciences, Kyushu University, Fukuoka, Japan; [4]Department of Radiation Oncology and Image-Applied Therapy, Kyoto University Graduate School of Medicine, Kyoto University, Kyoto, Japan; and [5]Biomedical Imaging Research Center, University of Fukui, Fukui, Japan

Hypoxia-inducible factor-1 (HIF-1) plays an important role in malignant tumor progression and in the development of resistance to radiotherapy. We designed a novel fusion protein (PTD-ODD-SAV [POS]) consisting of a protein transduction domain (PTD), streptavidin (SAV), and a portion of the oxygen-dependent degradation domain (ODD) of HIF-1α that confers the same oxygen-dependent regulation as HIF-1α on POS. (3-$^{123/125}$I-iodobenzoyl)norbiotinamide ($^{123/125}$I-IBB) was conjugated to the SAV moiety of POS to synthesize $^{123/125}$I-IBB-labeled POS ($^{123/125}$I-IPOS). The purpose of this study was to evaluate the feasibility of ^{123}I-IPOS as an imaging probe for HIF-1-active tumor hypoxia. **Methods:** After a 24-h incubation of ^{125}I-IPOS with various tumor cell lines under either normoxic (20% O_2) or hypoxic (0.1% O_2) conditions, the intracellular radioactivity was investigated. Then, the biodistribution of $^{123/125}$I-IPOS was examined with tumor-implanted mice, and an in vivo imaging study was performed. The tumoral accumulation of ^{125}I-IPOS was compared with HIF-1 activity using the mice carrying tumors with the HIF-1-dependent luciferase reporter gene. Furthermore, the intratumoral localization of ^{125}I-IPOS was examined by the autoradiographic study, and then the same slide was subjected to immunostaining for pimonidazole, which is the hypoxic marker. **Results:** The ratios of radioactivity in hypoxic cells to that in normoxic cells were more than 2. These results indicate incorporation of ^{125}I-IPOS into these cells and degradation of ^{125}I-IPOS by normoxic tumor cells. In the biodistribution study, ^{125}I-IPOS accumulated in the tumor (1.4 ± 0.3 percentage injected dose per gram) 24 h after administration. At that time, ^{125}I-IPOS showed high tumor-to-blood and tumor-to-muscle ratios (5.1 ± 0.3 and 14.0 ± 3.9, respectively). The tumors were clearly visualized by in vivo imaging 24 h after ^{123}I-IPOS injection (tumor-to-muscle ratio was 9.6). The tumoral accumulation of ^{125}I-IPOS correlated with HIF-1 activity ($R = 0.71$, $P < 0.05$), and its intratumoral distribution coincided with the hypoxic regions. **Conclusion:** ^{123}I-IPOS is a potential probe for the imaging of HIF-1 activity in tumors. Given the role of HIF-1 in tumor biology, its detection may be considered an indicator of aggressive cancer phenotypes.

Key Words: molecular imaging; oncology; radiopharmaceuticals; hypoxia-inducible factor-1 (HIF-1); tumor hypoxia; oxygen-dependent degradation (ODD); protein transduction domain (PTD)

J Nucl Med 2009; 50:942–949
DOI: 10.2967/jnumed.108.061119

In solid tumors, hypoxia, or an oxygen tension below physiologic levels, develops as abnormal proliferation outstrips the blood supply (*1*). This hypoxic region is involved in tumor malignancy and proliferation and results in the development of resistance to radiotherapy (*2–4*). Hypoxia-inducible factor-1 (HIF-1), a transcription factor that regulates the cellular response to hypoxia, induces several genes that mediate these changes in tumor behavior (*5,6*). Indeed, HIF-1-active or hypoxic cells have recently been shown to play crucial roles in angiogenesis and radioresistance (*7*). Finally, the expression level of HIF-1 correlates with a poor prognosis in many tumors (*8,9*). Thus, imaging HIF-1-active regions in a tumor has the potential to provide, in a noninvasive manner, insight into those aspects of tumor biology most relevant to treatment design.

HIF-1 is a heterodimer that consists of the oxygen-sensitive α-subunit (HIF-1α) and the constitutively expressed β-subunit (HIF-1β). Under normoxic conditions, HIF-1α is hydroxylated by prolyl hydroxylases on the proline residues in the oxygen-dependent degradation domain (ODD). The hydroxylated proline residues accelerate ubiquitination of ODD

Received Dec. 14, 2008; revision accepted Feb. 16, 2009.
For correspondence or reprints contact: Hideo Saji, Department of Patho-Functional Bioanalysis, Graduate School of Pharmaceutical Sciences, Kyoto University, 46-29 Yoshida-Shimo-Adachi-cho, Sakyo-ku, Kyoto 606-8501, Japan.
E-mail: hsaji@pharm.kyoto-u.ac.jp

and subsequent degradation of HIF-1α (*10*). HIF-1α expression is regulated in an oxygen-dependent manner at the posttranscriptional level and is responsible for regulation of HIF-1 activity (*11*).

We recently developed TOP3 (TAT-ODD-procaspase-3), a fusion protein with 3 domains: TAT-PTD, ODD, and procaspase-3 (*12–16*). The protein transduction domain (PTD) is derived from the PTD of the HIV type 1 TAT protein (*17*) and efficiently delivers TOP3 to any tissue in vivo. The ODD domain contains a von Hippel Lindau–mediated protein destruction motif of human HIF-1α protein (*18*) and confers hypoxia-dependent stabilization on TOP3 (*14*). Intraperitoneal injection of TOP3 into tumor-bearing mice results in specific targeting of HIF-1-active tumor cells (*7,12*). These results demonstrated that PTD-ODD fusion proteins were efficiently delivered to hypoxic regions and stabilized in HIF-1-active cells.

In this study, we took advantage of the PTD-ODD fusion proteins for imaging of HIF-1-active hypoxic tumors. To label PTD-ODD with a radioactive reagent, PTD3-ODD was fused to a monomeric streptavidin (SAV). The SAV component was then used to join the compound to a radiolabeled biotin derivative, (3-^{123}I-iodobenzoyl)norbiotinamide (^{123}I-IBB). Our concept of hypoxia imaging is summarized in Figure 1. In this study, we evaluated the feasibility of ^{123}I-IBB-labeled PTD-ODD-SAV (^{123}I-IPOS) as an imaging probe for HIF-1-active tumor hypoxia.

MATERIALS AND METHODS

Construction of Plasmid and Preparation of Recombinant Protein POS

To construct the pGEX/POS plasmid encoding the POS fusion protein, the cDNAs encoding PTD3 and $ODD_{548–603}$ were constructed as described previously (*18,19*). The cDNA encoding the spacer sequence VDVADLEHD was constructed by annealing synthesized oligonucleotides corresponding to the polypeptide to *Bgl*II and *Bam*HI endonuclease restriction sites at the 5′ and 3′ sites, respectively. SAV cDNA was amplified by polymerase chain reaction using corresponding oligonucleotides as primers and a bacterial genome as a template. The resultant cDNA encoded the SAV protein from its 25th amino acid to the C terminus and had *Kpn*I and *Xho*I endonuclease restriction sites at the 5′ and 3′ sites, respectively. The cDNA encoding POS was constructed by ligating the cDNAs constructed above into the *Eco*RI and *Xho*I sites of the pGEX-6P-3 vector (GE Healthcare Bioscience). The resultant pGEX/POS vector encoded GST-tagged POS and was transformed into BL21(DE3)plysS (Novagen). GST-POS recombinant protein was induced with 1 mM isopropyl-β-d-thiogalactopyranoside for 24 h at 4°C and purified over a glutathatione Sepharose 4B column (GE Healthcare Bioscience). The GST-tag was removed from the recombinant protein with PreScission Protease (GE Healthcare Bioscience) in the column. The eluate containing POS was then dialyzed against 10 mM Tris-hydrochloric acid buffer (pH 8.0) and concentrated using the Amicon Ultra-15 5k NMWL device (Millipore). The purity and molecular weight of POS were determined by sodium dodecylsulfate-polyacrylamide gel electrophoresis and Coomassie staining.

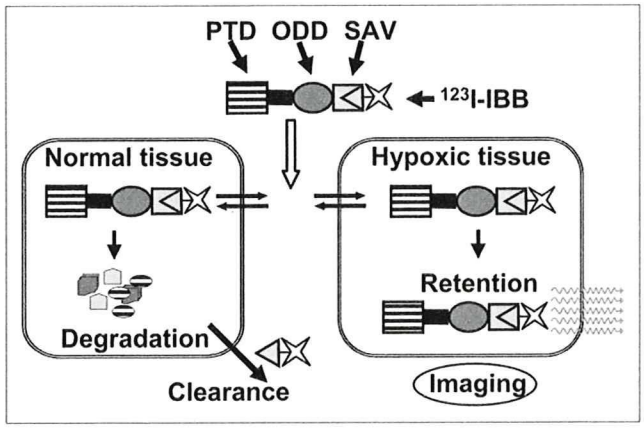

FIGURE 1. Concept of hypoxia imaging using ^{123}I-IPOS. PTD enables ^{123}I-IPOS to be delivered to normoxic and hypoxic tissue. In normoxic tissue, POS is degraded in manner similar to HIF-1α degradation, and ^{123}I-IBB is cleared. In contrast, in HIF-1-active tissues, POS escapes degradation and radioactivity is retained within cell. Thus, POS enables specific imaging of HIF-1-active hypoxic region.

Synthesis of IBB

IBB was prepared as previously described (*20*). The products were obtained as white crystals and stored under argon at 4°C (yield, 30.5%).

Radiosynthesis of ^{123}I-IBB and ^{125}I-IBB

Ammonium ^{123}I-iodide was kindly provided by Nihon Medi-Physics. Sodium ^{125}I-iodide was purchased from Perkin Elmer Life and Analytic Sciences. All other chemicals used were of reagent grade. A total of 1 GBq $NH_4{}^{123}I$ or 37 MBq $Na^{125}I$ were added to a vial containing *N*-succinimidyl 3-(tributhylstannyl)benzoate (72.2 μL, 2 mg/mL of 1% acetic acid methanol) and *N*-chlorosuccinimide (19.8 μL, 0.5 mg/mL of methanol). The vial was vortexed and the reaction allowed to proceed at room temperature for 30 min. $NaHSO_3$ (3.2 μL, 0.72 mg/mL in H_2O) was added to the product, which was vortexed before being concentrated under a stream of nitrogen. A solution of norbioinamine·hydrochloric acid in dimethylformamide:water (4:1) (100 μL, 3 mg/mL) was added to the vial. The reaction was incubated at room temperature for 2 h, and the sample was purified with high-performance liquid chromatography (HPLC) (Cosmosil $5C_{18}$-AR-300 column, 4.6 mm × 15 cm; Nacalai Tesque) (25% acetonitrile, 1 mL/min; wave length, 254 nm). The retention time of IBB was 21 min. The solvent was evaporated and was reconstituted in water for use in the in vitro and in vivo studies. The radiochemical purity was confirmed with HPLC using the same method as was used for purification.

Cell Culture

MM1, HeLa, and Suit2 cells were obtained from American Type Culture Collection. FM3A cells were purchased from the Health Science Research Resources Bank, and MDA-MB-231 cells were purchased from Dainippon Sumitomo Pharma Co., Ltd. MM1, HeLa, and Suit2/HRE-luciferase (*19*) cells were maintained in 10% fetal bovine serum–Dulbecco's modified Eagle's medium (Nissui Pharmaceutical). FM3A and MDA-MB-231 cells were cultured in 10% fetal bovine serum–RPMI medium (Nissui Pharmaceutical). The culture media were supplemented with penicillin (100 units/mL) and streptomycin (100 μg/mL). Cells were incubated at 37°C in

a well-humidified incubator with 5% CO_2 and 95% air for normoxic culture or incubated in an anaerobic chamber (Concept Mini MACS; Biotrace Limited) for hypoxic culture.

Binding of ^{125}I-IBB to POS

To prepare ^{125}I-IPOS, ^{125}I-IBB was added to a microtube containing POS (100 μL, 13.6 ng/mL). After a 1-h incubation, the reactant was purified by size-exclusion HPLC (TSKgel SuperSW2000 [4.6 mm × 30 cm] connected by the TSKguardcolumn SuperSW [4.6 mm × 3.5 cm]; Tosoh Corp.) (100 mM phosphate buffer [pH 6.8], 0.2 mL/min; wave length, 254 nm). The radiochemical purity was examined by paper chromatography developed with saline (R_f = 0).

Biotin Competitive Assay

^{125}I-IBB, D-biotin (0–40 pmol), and 100 mM citrate buffer (pH 5.0) were added to a microtube containing POS (1.36 ng). The reaction was performed at 37°C for 1 h. The reaction mixture was applied to an Amicon Microcon filter (Millipore) and centrifuged at 4°C and 4,500*g* for 30 min (Micro Cooling Centrifuge 1720; KUBOTA). The radioactivities of the reactant and filtrate were then measured and the binding rate calculated.

Cellular Assay

HeLa, MM1, and FM3A cells were transfected with the pGL3/5HRE-CMV_{mp}-luciferase plasmid, which induced luciferase expression in response to HIF-1 activity (*12*). Transfection was performed using reagent (Lipofectamin 2000; Invitrogen). After a 24-h incubation under normoxic (20% O_2) or hypoxic (0.1% O_2) conditions, cells were washed and lysed with Reporter Lysis Buffer (Promega), and luciferase activity was evaluated with a single tube luminometer (Lumat LB 9507; Berthold) using a Luciferase Assay System (Promega). The protein concentration was measured with the BCA Protein Assay Kit (Pierce) for normalization.

ODD-dependent, normoxic, POS degradation was evaluated by 2 assays. In the first assay, MM1, HeLa, and FM3A cells were incubated in advance for more than 6 h under either normoxic or hypoxic conditions, after which ^{125}I-IPOS (0.28 μg, 37 kBq) was added. Cells were then incubated for an additional 24 h in their respective culture conditions. After the cells were washed and lysed, the radioactivity of the lysate was measured using an auto well γ-counter (ARC2000; Aloka), and the protein concentration was measured and used for normalization. In the second assay, HeLa cells were incubated in advance for more than 6 h under hypoxic conditions, after which ^{125}I-IPOS (0.28 μg, 37 kBq) was added. The cells were then incubated for an additional 24 h under hypoxic conditions. After washing, the medium was replaced with fresh medium, and the cells were subjected to further incubation for 3 or 24 h under normoxic or hypoxic conditions. After the incubation, cells were washed and lysed, and the radioactivity and protein concentration of the lysate were measured. The radioactivities of the cells and medium were analyzed by ultrafiltration (Amicon Microcon filter; Millipore) and size-exclusion HPLC. All measurements were performed in triplicate.

Animal Model

Animal studies were conducted in accordance with our institutional guidelines, and the experimental procedures were approved by the Kyoto University Animal Care Committee. To produce the mouse models of tumor implantation, 5×10^6 FM3A cells in 100 μL of phosphate-buffered saline (PBS) were subcutaneously implanted into the right thighs of 5-wk-old female C3H/He mice (Japan SLC, Inc.). A total of 1×10^7 MDA-MB-231 cells or 5×10^6 Suit2/HRE-luciferase cells in 100 μL of PBS were subcutaneously implanted into the right thighs of 5-wk-old female BALB/c *nu/nu* mice (Japan SLC, Inc.). After the cells implanted, the mice were maintained on the AIN76-A–based biotin-free diet (Japan SLC, Inc.). FM3A and Suit2 tumor models were used 2 wk after implantation, and the MDA-MB-231 tumor models were used 1 mo after implantation for the tracer study.

Biodistribution

^{125}I-IPOS (0.05–30 μg, 37 kBq/mouse) or ^{125}I-IBB (37 kBq/mouse) was injected intravenously into FM3A-implanted mice. At the appropriate time points after administration, the mice were sacrificed. Whole-organ specimens were immediately removed and weighed, and the radioactivity was measured. The results were expressed as the percentage injected dose per gram (%ID/g).

In Vivo Imaging

^{123}I-IPOS (30 μg, 5.4–16 MBq) was injected in FM3A-implanted mice via the tail vein. The mice were anesthetized with 2.5% halothane and placed on the scanner bed in the prone position. Planar images were obtained for 10 min at 24 and 48 h after injection as previously described (*21*). Regions of interest were set on the tumor in the right thigh and the corresponding area in the left thigh.

Tumoral Accumulation of ^{125}I-IPOS Versus HIF-1 Transcriptional Activity in Vivo

The Suit2/HRE-luciferase–implanted mice were intravenously injected with ^{125}I-IPOS (30 μg, 37 kBq/mouse). After 24 h, 200 μL of D-luciferin solution (10 mg/mL in PBS; Promega) was injected intraperitoneally. After 20 min, the mice were anesthetized with 2.5% isoflurane and imaged using the IVIS Spectrum System (Xenogen) to measure the luciferase activity as the externally detected photon count. The photon counts within the tumors were analyzed with software (Living Image 3.0; Xenogen). After luciferase imaging, the mice were sacrificed and the tumors immediately removed. The radioactivity was then measured and the results expressed as the percentage injected dose (%ID).

Autoradiography

Autoradiographic studies of ^{125}I-IPOS were performed in MDA-MB-231–implanted mice. ^{125}I-IPOS (30 μg, 2.5 MBq/mouse) was injected intravenously, and at 22 h after injection pimonidazole (60 mg/kg) was injected intraperitoneally. Mice were sacrificed 2 h later. Autoradiograms were obtained as previously described (*21*), with the following slight modification: BAS5000 instead of BAS3000.

Immunohistochemistry

The slides used in the autoradiographic study were subjected to immunostaining for pimonidazole. The immunostaining was performed using the Hypoxyprobe-1 Plus Kit (Chemicon), according to the manufacturer's protocol. To evaluate the specificity of the signal, tumor sections derived from pimonidazole-untreated mice were also stained by following the same protocol.

Statistical Analyses

Comparisons between 2 groups were performed with the Mann–Whitney *U* test. Correlation coefficients were assessed using the Spearman rank analysis. A *P* value of less than 0.05 was considered statistically significant.

RESULTS

Construction of the Fusion Protein POS

The recombinant protein POS consisted of 3 parts: PTD, ODD, and SAV (Fig. 1). The PTD was composed of polylysine and hydrophobic amino acids, and was named PTD3. The ODD was $ODD_{548–603}$, the same as the one previously described in TOP3 (*7*). The spacer sequence VDVADLEHD was inserted between PTD and ODD for stabilization of the fusion protein. The molecular weight of the fusion protein was approximately 34 kDa (Fig. 2).

Radiosynthesis of ^{125}I-IBB and ^{123}I-IBB

^{125}I-IBB and ^{123}I-IBB were obtained in the absence of a carrier and with radiochemical yields of 65% and 29% and radiochemical purities of greater than 94% and greater than 95%, respectively (Supplemental Fig. 1; supplemental materials are available online only at http://jnm.snmjournals.org).

Binding of ^{125}I-IBB to POS

After the incubation of ^{125}I-IBB with POS, the radioactivity was detected at about 34 kDa by size-exclusion HPLC analysis, indicating that ^{125}I-IBB bound to POS to form ^{125}I-IPOS (Fig. 3A). This binding was inhibited by D-biotin in a dose-dependent manner (Fig. 3B).

Oxygen-Dependent Regulation of ^{125}I-IPOS In Vitro

To validate the stabilization of HIF-1α in our experimental conditions, we performed a luciferase assay using an HRE-responsive reporter system (*12*). The luciferase activities in HeLa, MM1, and FM3A cells, incubated under hypoxic conditions, were 28-, 17- and 29-fold higher than those of cells incubated under normoxic conditions, respectively (Fig. 4A).

We then added ^{125}I-IPOS to the culture medium of HeLa, MM1, and FM3A cells and compared the radioactivity retained in the cells after incubation under normoxic conditions with that after incubation under hypoxic conditions for 24 h. The ratios of the radioactivity in hypoxic cells to that in normoxic cells were 2.7, 2.2, and 2.3 in HeLa, MM1, and FM3A cells, respectively (Fig. 4B). Furthermore, the accumulated radioactivity under hypoxic conditions was decreased in a time-dependent manner after reoxygenation. After 24-h reoxygenation, the ratio of the radioactivity in hypoxic cells to that in reoxygenated cells was 1.8 ± 0.3 (Fig. 4C). The size-exclusion HPLC analysis revealed that more than 80% of the intracellular radioactivity was derived from intact ^{125}I-IPOS, and that approximately 70% of radioactivity in the reoxygenated medium was derived from ^{125}I-IBB and other small molecules (data not shown).

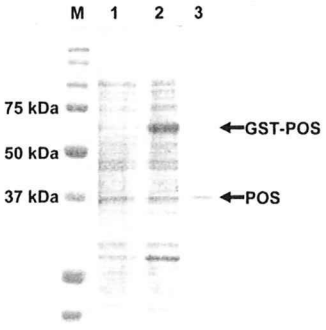

FIGURE 2. Analysis of fusion protein expression with sodium dodecylsulfate-polyacrylamide gel electrophoresis (lane M, molecular weight marker; lane 1, *Escherichia coli* lysate before IPTG induction; lane 2, *E. coli* lysate after IPTG induction; lane 3, protein solution after purification). New band was expressed in lane 2 at about 60 kDa, corresponding to GST-fused POS. After purification, only 1 band was detected in lane 3 at 34 kDa. IPTG = isopropyl-β-d-thiogalactopyranoside.

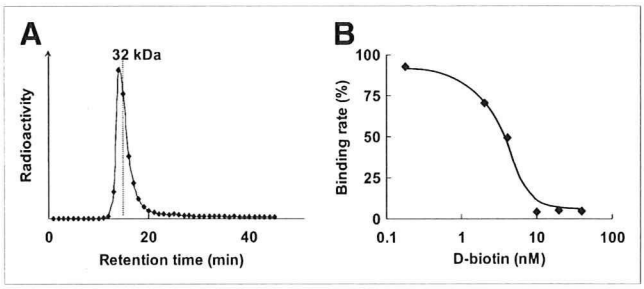

FIGURE 3. Binding of ^{125}I-IBB to POS. (A) Size-exclusion HPLC chromatogram after incubation of ^{125}I-IBB with POS. Symbols represent radioactivity of each eluate collected every 1 min. (B) Concentration-dependent inhibition of ^{125}I-IBB binding to POS by D-biotin. Symbols and bars represent mean and SD.

Biodistribution

When we examined the biodistribution of ^{125}I-IBB alone, the tumor-to-blood ratio was always less than 1 at each time point, indicating no tumor accumulation of ^{125}I-IBB (data not shown). Next, we performed a biodistribution study of ^{125}I-IPOS. A high level of radioactivity accumulated in the liver and the spleen, and a moderate level was present in the intestine and the kidneys. Though the radioactivity in the blood at 1 h after injection was higher than the corresponding data for ^{125}I-IBB (*20*), blood clearance was rapid. In contrast, the radioactivity tended to be retained in the tumor (1.47 %ID/g at 1 h and 1.49 %ID/g at 6 h). The tumor-to-blood ratio was greater than 1 at 24 h or more after injection (Table 1). We then evaluated whether the accumulation of ^{125}I-IPOS in the tumor was dose-dependent. There were no differences in the tumor accumulation and the tumor-to-blood ratio between the 0.05- and the 0.5-μg injected groups. However, a dose-dependent increase was observed when more than 0.5 μg of ^{125}I-IPOS was injected. The tumor accumulation and tumor–to–normal tissue ratio were highest in the 30-μg injected group (Table 2). The tumor accumulation was 1.4 %ID/g, the tumor-to-blood ratio was 5.1, and the tumor-to-muscle ratio was 14.0 at 24 h after injection (Table 2). Evaluation 48 h after injection demonstrated further increases in the tumor-to-blood ratio and the tumor-to-muscle ratio (12.8 and 22.3, respectively; data not shown).

In Vivo Imaging

The tumor was clearly visualized both at 24 and at 48 h after ^{123}I-IPOS injection (Fig. 5). At 24 and 48 h after

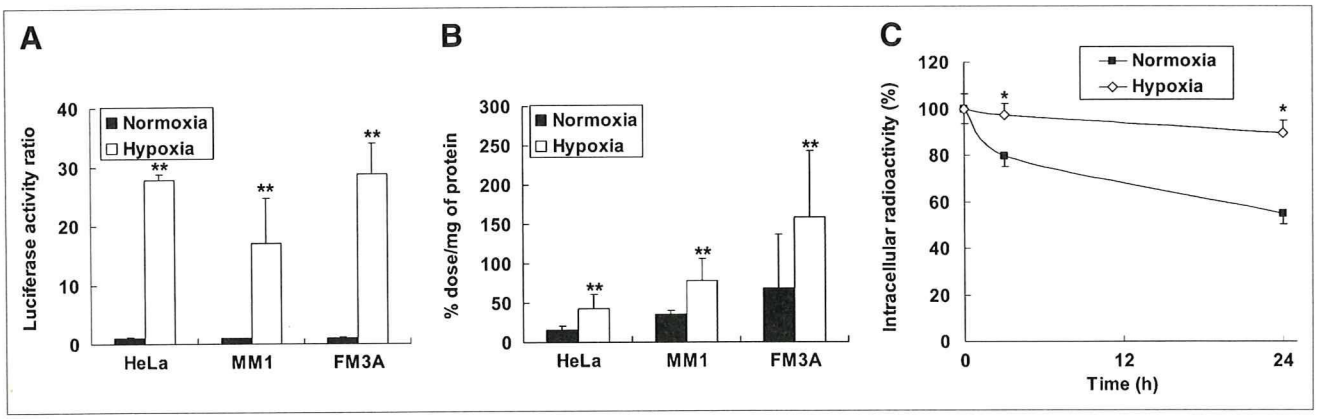

FIGURE 4. (A) HIF-1-dependent luciferase activity in HeLa, MM1, and FM3A cells. Data were normalized by protein concentration of cells. Results are shown as ratio of activity after hypoxia to activity after normoxia. Columns and bars represent mean and SD (n = 3–6 $^{**}P < 0.01$ vs. normoxia). (B) Intracellular radioactivity in HeLa, MM1, and FM3A cells after 24-h incubation under either normoxic or hypoxic conditions. Radioactivity was normalized by protein concentration of cells. Columns and bars represent mean and SD (n = 3–6 $^{**}P < 0.01$ vs. normoxia). (C) Degradation of intracellularly accumulated IPOS after reoxygenation. HeLa cells were incubated with ^{125}I-IPOS for 24 h under hypoxic conditions. Then, medium was replaced with fresh medium, and cells were subjected to further incubation under normoxic or hypoxic conditions. Results are shown as percentage of radioactivity at start of second incubation. Symbols and bars represent mean and SD (n = 3–5; $^{*}P < 0.05$ vs. normoxia).

injection, the calculated tumor-to-muscle ratios were 9.6 ± 4.7 and 20 ± 21, respectively (n = 6). Although the accumulation of ^{123}I-IPOS in the abdominal region was high, there was little accumulation in the thoracic region.

Comparison Between Tumoral Accumulation of ^{125}I-IPOS and HIF-1 Activity In Vivo

Figure 6 shows the highly significant correlation between luciferase activity and radioactivity (R = 0.71, $P < 0.05$).

Regional Distribution of ^{125}I-IPOS Relative to Hypoxic Regions in Tumor

Pimonidazole immunohistochemistry demonstrated hypoxic areas within the tumor (Fig. 7B). On the other hand, the section derived from pimonidazole-untreated mice was not stained (Fig. 7D). The autoradiogram represents the distribution of ^{125}I-IPOS in the tumor and shows that the distribution is heterogeneous and for the most part corresponds to the pimonidazole-positive hypoxic areas. However, there were also a few pimonidazole-positive regions that did not show accumulation of ^{125}I-IPOS (Figs. 7A and 7C).

DISCUSSION

HIF-1, which is activated by hypoxia, is associated with an aggressive cancer phenotype. Tumors expressing HIF-1 are resistant to radiation therapy and chemotherapy and as a result carry a poor prognosis. Noninvasive imaging of HIF-1 activity is of great interest because it may be used to predict prognosis. In our present study, we found that POS entered into tumor cells and was degraded in an oxygen-dependent manner, $^{123/125}$I-IPOS accumulated in tumors and the tumors were clearly visualized by in vivo imaging, the tumoral accumulation of ^{125}I-IPOS correlated with tumoral HIF-1

TABLE 1. Biodistribution of ^{125}I-IPOS in FM3A-Implanted Mice

Organ	Time after injection (h)			
	1	6	24	48
Blood	15.55 ± 1.06	3.14 ± 0.54	0.18 ± 0.12	0.01 ± 0.01
Liver	32.97 ± 1.03	13.80 ± 0.87	0.97 ± 0.44	0.30 ± 0.06
Spleen	17.29 ± 2.35	6.07 ± 0.73	1.21 ± 0.53	0.19 ± 0.05
Kidney	5.51 ± 0.36	2.79 ± 0.47	0.74 ± 0.60	0.09 ± 0.02
Stomach	2.25 ± 0.57	0.62 ± 0.32	0.49 ± 0.31	0.04 ± 0.02
Neck	2.39 ± 0.06	0.80 ± 0.08	0.09 ± 0.04	0.00 ± 0.01
Intestine	7.96 ± 0.09	9.82 ± 1.61	0.91 ± 0.13	0.24 ± 0.08
Tumor	1.47 ± 1.02	1.49 ± 0.38	0.28 ± 0.08	0.07 ± 0.05
Muscle	0.94 ± 0.65	0.28 ± 0.05	0.07 ± 0.06	0.00 ± 0.01
Tumor/blood	0.10 ± 0.07	0.49 ± 0.18	1.79 ± 0.59	6.72 ± 6.61

Organ uptake values are expressed as %ID/g of tissue except for tumor/blood. Values are mean ± SD; n = 3–5.

TABLE 2. Effect of POS Concentration on Biodistribution of ^{125}I-IPOS in FM3A-Implanted Mice at 24 Hours After Injection

Organ	Protein concentration (μg)			
	0.05	0.5	5	30
Blood	0.12 ± 0.04	0.16 ± 0.10	0.16 ± 0.01	0.27 ± 0.07
Liver	1.92 ± 0.24	1.27 ± 0.53	5.53 ± 1.05	13.61 ± 1.90
Spleen	1.07 ± 0.30	1.15 ± 0.41	2.33 ± 0.25	7.87 ± 2.20
Kidney	0.35 ± 0.20	0.59 ± 0.51	1.03 ± 0.10	4.32 ± 1.87
Stomach	0.28 ± 0.14	0.55 ± 0.42	0.52 ± 0.20	0.86 ± 0.27
Neck	0.05 ± 0.04	0.09 ± 0.04	0.11 ± 0.02	0.23 ± 0.08
Intestine	4.57 ± 0.82	1.95 ± 2.03	2.17 ± 0.24	2.18 ± 0.28
Tumor	0.23 ± 0.08	0.25 ± 0.07	0.49 ± 0.09	1.37 ± 0.33
Muscle	0.05 ± 0.03	0.05 ± 0.05	0.07 ± 0.01	0.10 ± 0.03
Tumor/blood	2.04 ± 0.61	1.61 ± 0.10	3.00 ± 0.68	5.14 ± 0.34

Organ uptake values are expressed as %ID/g of tissue except for tumor/blood. Values are mean ± SD; $n = 5$.

activity, and the intratumoral distribution of ^{125}I-IPOS corresponded to the hypoxic regions. These findings demonstrate the feasibility of ^{123}I-IPOS as an imaging probe for HIF-1-active, hypoxic tumors. ^{123}I-IPOS is the first nuclear medical imaging probe for the detection of HIF-1 activity in vivo.

Other hypoxia imaging probes such as ^{18}F-fluoromisonidazole (^{18}F-FMISO) and ^{64}Cu-diacetyl-bis(*N4*-methylthiosemicarbazone) (^{64}Cu-ATSM) have been reported previously. The retention mechanism of both of these probes in the hypoxic regions is based on reduction reactions and the formation of covalent bonds to intracellular macromolecules (*22*). ^{18}F-FMISO uptake is increased only when oxygen levels fall below 2–3 mm Hg (*23*). The uptake of ^{64}Cu-ATSM is also markedly increased in a sigmoidal fashion under hypoxic and anoxic conditions (<3.8 mm Hg) (*24,25*). Previous immunohistochemical study showed that HIF-1α is more frequently present adjacent to blood vessels than in the pimonidazole-positive regions (*26*), and the pO_2 in the HIF-1-active regions is approximately 10–15 mm Hg (*27*). Thus, neither ^{18}F-FMISO nor ^{64}Cu-ATSM is suitable for completely monitoring HIF-1 activity. Recently it was reported that the expression level of HIF-1 correlates with a poor prognosis in many tumors (*8,9*). Thus, imaging HIF-1-active regions in a tumor using ^{123}I-IPOS has the potential to provide insight into those aspects of tumor biology most relevant to treatment design.

Protein transduction with the PTD has proven to be an effective way of delivering proteins in vitro, and recently several reports have also shown valuable in vivo applications for protein transduction in correcting disease states (*28*). A positive charge is important for the cellular membrane permeability of PTD. Moreover, lysine residues are required for efficient ubiquitination and after degradation of HIF-1α (*29*). Therefore, we combined a poly-lysine sequence with a hydrophobic polypeptide to construct a unique PTD, PTD3. We characterized PTD3 in a prior study (*19*).

Because of its extremely high affinity and in vivo stability, we used the SAV-biotin system for radiolabeling the protein. Because the binding of ^{125}I-IBB to POS was inhibited in a concentration-dependent manner by D-biotin (Fig. 2B), it was evident that ^{125}I-IBB bound to the SAV moiety of POS, as was expected. Biotinylated probes have been used for other imaging modalities including fluorescent dyes (*30*) and gadolinium dendrimers (*31*). Thus, POS would have applications not only in nuclear medical imaging but also in optical imaging and MRI.

The luciferase activity in the hypoxic conditions was significantly higher than that in normoxic conditions (Fig. 4A), which indicates that the experimental settings used here to induce hypoxia are suitable for HIF-1α stabilization. After incubation of the cells with ^{125}I-IPOS under normoxic or hypoxic conditions, higher radioactivity was retained in the cells incubated under hypoxic conditions (Fig. 4B), and

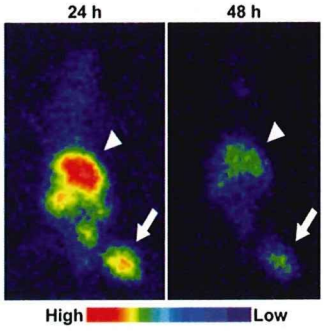

FIGURE 5. Typical planar images of FM3A-implamted mice at 24 or 48 h after injection of ^{123}I-IPOS. Tumors were clearly visualized in both images (arrow). Arrowheads indicate liver.

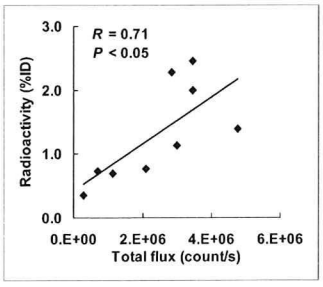

FIGURE 6. Correlation between accumulation of ^{125}I-IPOS and HIF-1 activity within same tumor. Ordinate represents accumulated radioactivity (%ID), and abscissa represents HIF-1-dependent luciferase activity. Correlation coefficient (R) was 0.71, indicating highly significant correlation ($P < 0.05$).

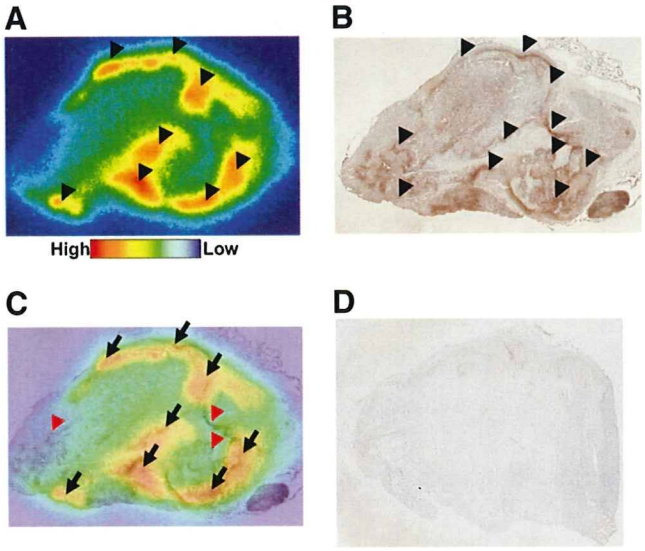

FIGURE 7. Comparison between intratumoral distribution of ^{125}I-IPOS and pimonidazole-positive hypoxic region. Typical autoradiogram (A) and pimonidazole immunohistochemical staining (B) in identical section are shown. Merged image (C) is also presented. Black arrowheads indicate area of ^{125}I-IPOS accumulation in A and pimonidazole-positive area in B. Black arrows show areas in which both signals are positive, and red arrowheads indicate pimonidazole-positive areas without accumulation of ^{125}I-IPOS. No signal was observed in pimonidazole-untreated tumor (D).

intracellular radioactivity under normoxic conditions decreased more rapidly than that under hypoxic conditions (Fig. 4C). The size-exclusion HPLC analysis revealed that the intracellular radioactivity was mostly derived from intact ^{125}I-IPOS and that the radioactivity in the reoxygenated medium was derived from ^{125}I-IBB and other small molecules. Thus, the difference in intracellular radioactivity under normoxic and hypoxic conditions probably reflects the oxygen-dependent degradation of POS, followed by clearance of ^{125}I-IBB from the normoxic cells. Because ^{125}I-IBB is a small molecule and has adequate lipophilicity for membrane transportation, it could be cleared rapidly. However, appreciable radioactivity remained after 24-h incubation under normoxic conditions (Figs. 4B and 4C). Though POS contains the essential domain related to the oxygen-dependent degradation of HIF-1α, it contains PTD and SAV as well. These modifications may lower the rate of degradation.

After injection of ^{125}I-IPOS, high levels of radioactivity were detected in the liver, intestine, and kidneys. Because other constructs incorporating the PTD-ODD fusion proteins or SAV separately did not accumulate in the liver, the fusion of PTD-ODD with SAV may be responsible for hepatic accumulation. Multiple factors, such as molecular size, electrical charge, and slow blood clearance, may be involved. The accumulation in the kidneys may reflect either the propensity of SAV to localize in the kidneys (*32*) or the high HIF-1 activity in the kidneys (*33*). Radioactivity did not accumulate in either the stomach or the thyroid, which demonstrates the resistance of ^{125}I-IPOS to in vivo deiodination. Tumor accumulation of ^{125}I-IPOS increased in a concentration-dependent manner (Table 2). As the administered concentration increased, oxygen-dependent degradation mechanisms in the normal tissues were overwhelmed, thereby increasing the quantity of POS delivered to the tumor.

In vivo imaging revealed that the tumor accumulation of ^{123}I-IPOS correlated with HIF-1 activity. The background radioactivity in the thoracic region was quite low. Thus, ^{123}I-IPOS would be particularly useful for detecting HIF-1 activity in lung and breast tumors. The expression of HIF-1 correlates with a poor prognosis in breast tumors (*34*); therefore, ^{123}I-IPOS may be useful for the noninvasive determination of prognosis.

In the autoradiographic study, there were a few pimonidazole-positive regions in which ^{125}I-IPOS did not accumulate. Regions in which there is no accumulation could be explained by a difference in molecular size. The significantly smaller size of pimonidazole may enable its more efficient delivery to hypoxic tissues than the larger POS. Another possible explanation is the time lag between probe injections. In the present study, ^{125}I-IPOS was injected 22 h before the injection of pimonidazole. The microenvironment in tumors changes dynamically. If the oxygen level of a normoxic region decreased after the degradation of ^{125}I-IPOS, pimonidazole would be able to accumulate in the region. These explanations also indicate the limitations of ^{123}I-IPOS. The slow kinetics due to its molecular size and the necessity of prolonged time for degradation will prevent imaging of acute hypoxic regions with ^{123}I-IPOS. However, it should be emphasized that ^{125}I-IPOS mainly accumulated both in the pimonidazole-positive regions and in the regions surrounding them. This result is consistent with the previous results that HIF-1 expresses at higher levels of oxygen than those that allow pimonidazole metabolism and binding (*26*). Thus, the area in which ^{125}I-IPOS accumulates possibly corresponds to the HIF-1-active hypoxic region.

We confirmed the specific localization of the PTD-ODD fusion protein to HIF-1-active cells using optical imaging techniques (*7,12*). We recently constructed a novel optical imaging probe with the PTD-ODD fusion protein. We then successfully used this probe to obtain specific images of HIF-1-active cells in the ischemic brain of the focal stroke mouse model and of subcutaneous tumors in nude mice. These results further strengthen the argument that PTD-ODD fusion proteins including IPOS are efficiently delivered to hypoxic regions and stabilized in HIF-1-active cells.

CONCLUSION

We have developed a POS fusion protein containing the ODD domain of human HIF-1α. POS was degraded in an oxygen-dependent manner and was stabilized in the cells in which HIF-1 was active. Furthermore, ^{123}I-IPOS enabled the clear visualization of the tumor in vivo and its accumulation

correlated with HIF-1 activity in these tumors. These results support a possible role for ^{123}I-IPOS in the imaging of HIF-1-active tumor hypoxia.

ACKNOWLEDGMENTS

We thank Nihon Medi-Physics for providing the ammonium ^{123}I-iodide. We are grateful to Hiroaki Konishi for skilled technical assistance. This study was supported in part by Health Labour Sciences Research Grant for Research on Advanced Medical Technology, from The Ministry of Health, Labour and Welfare of Japan, and a Grant-in-Aid for Exploratory Research (17659010) from The Ministry of Education, Culture, Sports, Science and Technology of Japan.

REFERENCES

1. Vaupel P, Kallinowski F, Okunieff P. Blood-flow, oxygen and nutrient supply, and metabolic microenvironment of human-tumors: a review. *Cancer Res.* 1989;49:6449–6465.
2. Brown JM. Exploiting the hypoxic cancer cell: mechanisms and therapeutic strategies. *Mol Med Today.* 2000;6:157–162.
3. Hockel M, Vaupel P. Tumor hypoxia: definitions and current clinical, biologic, and molecular aspects. *J Natl Cancer Inst.* 2001;93:266–276.
4. Teicher BA. Hypoxia and drug resistance. *Cancer Metastasis Rev.* 1994;13:139–168.
5. Semenza GL. Expression of hypoxia-inducible factor 1: mechanisms and consequences. *Biochem Pharmacol.* 2000;59:47–53.
6. Wenger RH. Cellular adaptation to hypoxia: O_2-sensing protein hydroxylases, hypoxia-inducible transcription factors, and O_2-regulated gene expression. *FASEB J.* 2002;16:1151–1162.
7. Harada H, Kizaka-Kondoh S, Li G, et al. Significance of HIF-1-active cells in angiogenesis and radioresistance. *Oncogene.* 2007;26:7508–7516.
8. Marignol L, Coffey M, Lawler M, Hollywood D. Hypoxia in prostate cancer: a powerful shield against tumour destruction? *Cancer Treat Rev.* 2008;34:313–327.
9. Miyake K, Yoshizumi T, Imura S, et al. Expression of hypoxia-inducible factor-1α, histone deacetylase 1, and metastasis-associated protein 1 in pancreatic carcinoma: correlation with poor prognosis with possible regulation. *Pancreas.* 2008;36:e1–e9.
10. Bruick RK, McKnight SL. A conserved family of prolyl-4-hydroxylases that modify HIF. *Science.* 2001;294:1337–1340.
11. Wang GL, Jiang BH, Rue EA, Semenza GL. Hypoxia-inducible factor 1 is a basic-helix-loop-helix-PAS heterodimer regulated by cellular O_2 tension. *Proc Natl Acad Sci USA.* 1995;92:5510–5514.
12. Harada H, Kizaka-Kondoh S, Hiraoka M. Optical imaging of tumor hypoxia and evaluation of efficacy of a hypoxia-targeting drug in living animals. *Mol Imaging.* 2005;4:182–193.
13. Kizaka-Kondoh S, Inoue M, Harada H, Hiraoka M. Tumor hypoxia: a target for selective cancer therapy. *Cancer Sci.* 2003;94:1021–1028.
14. Harada H, Hiraoka M, Kizaka-Kondoh S. Antitumor effect of TAT-oxygen-dependent degradation-caspase-3 fusion protein specifically stabilized and activated in hypoxic tumor cells. *Cancer Res.* 2002;62:2013–2018.
15. Kageyama Y, Sugiyama H, Ayame H, et al. Suppression of VEGF transcription in renal cell carcinoma cells by pyrrole-imidazole hairpin polyamides targeting the hypoxia responsive element. *Acta Oncol.* 2006;45:317–324.
16. Inoue M, Mukai M, Hamanaka Y, Tatsuta M, Hiraoka M, Kizaka-Kondoh S. Targeting hypoxic cancer cells with a protein prodrug is effective in experimental malignant ascites. *Int J Oncol.* 2004;25:713–720.
17. Schwarze SR, Ho A, Vocero-Akbani A, Dowdy SF. In vivo protein transduction: delivery of a biologically active protein into the mouse. *Science.* 1999;285:1569–1572.
18. Harada H, Kizaka-Kondoh S, Hiraoka M. Mechanism of hypoxia-specific cytotoxicity of procaspase-3 fused with a VHL-mediated protein destruction motif of HIF-1α containing Pro564. *FEBS Lett.* 2006;580:5718–5722.
19. Kizaka-Kondoh S, Itasaka S, Zeng L, et al. Selective killing of hypoxia-inducible factor-1-active cells improves survival in a mouse model of invasive and metastatic pancreatic cancer. *Clin Cancer Res.* In press.
20. Foulon CF, Alston KL, Zalutsky MR. Synthesis and preliminary biological evaluation of (3-iodobenzoyl)norbiotinamide and ((5-iodo-3-pyridinyl)carbonyl)norbiotinamide: two radioiodinated biotin conjugates with improved stability. *Bioconjug Chem.* 1997;8:179–186.
21. Ishino S, Kuge Y, Takai N, et al. ^{99m}Tc-annexin A5 for noninvasive characterization of atherosclerotic lesions: imaging and histological studies in myocardial infarction-prone Watanabe heritable hyperlipidemic rabbits. *Eur J Nucl Med Mol Imaging.* 2007;34:889–899.
22. Krohn KA, Link JM, Mason RP. Molecular imaging of hypoxia. *J Nucl Med.* 2008;49(suppl 2):129S–148S.
23. Rasey JS, Nelson NJ, Chin L, Evans ML, Grunbaum Z. Characteristics of the binding of labeled fluoromisonidazole in cells in vitro. *Radiat Res.* 1990;122:301–308.
24. Lewis JS, McCarthy DW, McCarthy TJ, Fujibayashi Y, Welch MJ. Evaluation of ^{64}Cu-ATSM in vitro and in vivo in a hypoxic tumor model. *J Nucl Med.* 1999;40:177–183.
25. Vavere AL, Lewis JS. Cu-ATSM: a radiopharmaceutical for the PET imaging of hypoxia. *Dalton Trans.* 2007;4893–4902.
26. Sobhanifar S, Aquino-Parsons C, Stanbridge EJ, Olive P. Reduced expression of hypoxia-inducible factor-1α in perinecrotic regions of solid tumors. *Cancer Res.* 2005;65:7259–7266.
27. Jiang BH, Semenza GL, Bauer C, Marti HH. Hypoxia-inducible factor 1 levels vary exponentially over a physiologically relevant range of O_2 tension. *Am J Physiol.* 1996;271:C1172–C1180.
28. Chauhan A, Tikoo A, Kapur AK, Singh M. The taming of the cell penetrating domain of the HIV Tat: myths and realities. *J Control Release.* 2007;117:148–162.
29. Paltoglou S, Roberts BJ. HIF-1α and EPAS ubiquitination mediated by the VHL tumour suppressor involves flexibility in the ubiquitination mechanism, similar to other RING E3 ligases. *Oncogene.* 2007;26:604–609.
30. Ebner A, Marek M, Kaiser K, et al. Application of biotin-4-fluorescein in homogeneous fluorescence assays for avidin, streptavidin, and biotin or biotin derivatives. *Methods Mol Biol.* 2008;418:73–88.
31. Zhu W, Okollie B, Bhujwalla ZM, Artemov D. PAMAM dendrimer-based contrast agents for MR imaging of Her-2/neu receptors by a three-step pretargeting approach. *Magn Reson Med.* 2008;59:679–685.
32. Forster GJ, Santos EB, Smith-Jones PM, Zanzonico P, Larson SM. Pretargeted radioimmunotherapy with a single-chain antibody/streptavidin construct and radiolabeled DOTA-biotin: strategies for reduction of the renal dose. *J Nucl Med.* 2006;47:140–149.
33. Safran M, Kim WY, O'Connell F, et al. Mouse model for noninvasive imaging of HIF prolyl hydroxylase activity: assessment of an oral agent that stimulates erythropoietin production. *Proc Natl Acad Sci USA.* 2006;103:105–110.
34. Trastour C, Benizri E, Ettore F, et al. HIF-1α and CA IX staining in invasive breast carcinomas: prognosis and treatment outcome. *Int J Cancer.* 2007;120:1451–1458.

Original Article

RhoA and Rac1 Changes in the Atherosclerotic Lesions of WHHLMI Rabbits

Hiroshi Ohkawara[1], Toshiyuki Ishibashi[1], Masashi Shiomi[2], Koichi Sugimoto[1], Hironori Uekita[1], Masashi Kamioka[1], Yoh Takuwa[3], Tamio Teramoto[4], Yukio Maruyama[1,5], and Yasuchika Takeishi[1]

[1]Department of Cardiology and Hematology, Fukushima Medical University, Fukushima, Japan
[2]Institute for Experimental Animals, Kobe University Graduate School of Medicine, Kobe, Japan
[3]Department of Molecular and Cellular Physiology, Kanazawa University Graduate School of Medical Sciences, Kanazawa, Japan
[4]Department of Internal Medicine, Teikyo University School of Medicine, Tokyo, Japan
[5]Hoshi General Hospital, Koriyama, Japan

Aim: The activation of RhoA and Rac1 is crucial for the pathogenesis of atherosclerosis. This study investigated the changes of unprocessed and mature forms of RhoA and Rac1 in the progression of atherosclerosis.
Methods: Unprocessed and geranylgeranylated forms of RhoA and Rac1 in aortic atherosclerotic lesions were separated by the Triton X-114 partition method using Watanabe heritable hyperlipidemic (WHHLMI) rabbits prone to myocardial infarction. The activation of RhoA and Rac1 was determined by membrane translocation and pull-down assays.
Results: The levels of unprocessed RhoA and Rac1 of the aortas were higher at 7 months than 3 months, accompanied by increased levels of total RhoA and Rac1. Membrane-bound RhoA and Rac1 levels of the aortas at 7 months were significantly increased compared with those at 3 months, consistent with the results of GTP-loading. Unprocessed and activated forms of RhoA and Rac1 had gradually decreas at 15 and 24 months compared to 7 months.
Conclusions: We show evidence of marked increases in unprocessed RhoA and Rac1 with enhanced activities in the progression of atherosclerosis in WHHLMI rabbits. This is important for better understanding of the pathogenesis of hyperlipidemia-dependent atherosclerosis.

J Atheroscler Thromb, 2009; 16:846-856.

Key words; Atherosclerosis, Geranylgeranylation, GTP-loading

Introduction

In the Ras homolog gene family, member A (RhoA) is a small GTPase protein known to regulate the actin cytoskeleton in the formation of stress fibers. Rac1 (Ras-related C3 botulinum toxin substrate1) is a small (~21 kDa) GTPase protein, a member of the Rac subfamily of the Rho family of GTPases. This molecule is a pleiotropic regulator of many cellular processes including the cell cycle, cell-cell adhesion and motility through the actin network[1,2]. In the vascular wall, RhoA plays an important role in endothelial dysfunction, which is fundamental to the pathogenesis of atherosclerosis, whereas Rac1 is essential for the assembly and activation of NADPH oxidase, the major source of reactive oxygen species (ROS)[3-7]. Unprocessed and lipid-modified forms of RhoA and Rac1 exist in the cytoplasma. Activation of these small GTPases primarily consists of three steps, lipid modification (geranylgeranylation), GDP/GTP exchange (GTP-loading) and membrane translocation[1]. We previously reported the rapid activation of RhoA by lysophosphatidylcholine (LPC), a phospholipid component of oxidized low-density lipoprotein (LDL) in endothelial cells[8]. We also found that rapid geranylgeranylation plays an essential role for full activation

Address for correspondence: Toshiyuki Ishibashi, Department of Cardiology and Hematology, Fukushima Medical University, 1 Hikarigaoka, Fukushima 960-1295, Japan
E-mail: masaishi@fmu.ac.jp
Received: April 7, 2009
Accepted for publication: June 11, 2009

of unprocessed RhoA in thrombin-stimulated endothelial cells[9].

It has been shown that RhoA and Rac1 are expressed in the remodeled vascular wall *in vivo*[3, 10-12]. Protein levels of RhoA reportedly increase several-fold in an atherogenic animal model of apolipoprotein E-deficient mice compared with wild-type control mice[11]. Moreover, physical activity decreases Rac1 activity, ROS generation and atherosclerotic lesion formation in atherogenic mice[12]; however, little is known about the profiles of unprocessed and geranylgeranylated RhoA and Rac1 and the activities of these molecules in the progression of atherosclerosis.

This study investigated the proportions of unprocessed and geranylgeranylated RhoA and Rac1 as well as the activities of the two molecules in the progression of atherosclerosis using a novel atherosclerosis animal model of Watanabe heritable hyperlipidemic (WHHLMI) rabbits prone to myocardial infarction which spontaneously develop atherosclerosis[13, 14].

Methods

Materials

The sources of most conventional reagents for protein and immunohistochemical analyses were described previously[8, 9, 15, 16].

Animals

Male and female WHHLMI rabbits with no sex-related differences in atherosclerosis were bred at the Institute for Experimental Animals, Kobe University Graduate School of Medicine. The animals were kept in rooms equipped with laminar-flow filters at a temperature of ~22℃ and were fed standard rabbit chow in the Experimental Animal Laboratory of Fukushima Medical University[13, 15].

Study Protocol

Three- to 24-month-old WHHLMI rabbits were selected on the basis of their serum cholesterol levels, which ranged from 13.0 to 18.1 mmol/L, to make the degrees of atherosclerosis[13, 17]. Rabbits were euthanized by an intravenous injection of 50 mg/kg sodium pentobarbital. After perfusion-fixation, thoracic aortas of rabbits were removed and used for histological and immunohistochemical analyses of atheromatous plaques and the objectives described below. We examined the expression of RhoA and Rac1 in the aortas, as determined by fluorescent immunohistochemistry. Unprocessed and geranylgeranylated forms of RhoA and Rac1 of the aortas at the ages of 3, 7, 15 and 24 months were separated by the Triton X-114 partition method and their levels were determined by Western blotting. We performed membrane translocation and pull-down assays to determine the activities of RhoA and Rac1 of the aortas at 3, 7 and 15 months, whereas the activity of $p47^{phox}$, another component of NADPH oxidase, was determined by membrane translocation. These experiments were carried out under the control of the Animal Research Committee in accordance with the Guidelines on Animal Experiments of Fukushima Medical University and the Japanese Government Animal Protection and Management Law (No. 105), as well as the Guide for the Care and Use of Laboratory Animals (NIH Publication No. 85-23, revised 1996).

Histological Analysis

Rabbits were anesthetized and perfused with lactated Ringer's solution and then Bouin's fixative using perfusion apparatus at a constant pressure of 100 mmHg. After perfusion-fixation, atherosclerotic lesions of the aortas were excised and then immersed in Bouin's fixative for at least 24 hours. After immersion-fixation, atherosclerotic lesions were embedded in paraffin and cut into 4-μm-thick sections. The sections were used for Azan-Mallory and hematoxylin and eosin (H&E) staining, and fluorescent immunohistochemistry[13, 15].

Fluorescent Immunohistochemistry of RhoA and Rac1

The sections were incubated for 60 minutes at room temperature with mouse monoclonal antibodies against RhoA diluted 1:200 (Santa Cruz Biotechnology Inc., Santa Cruz, CA), Rac1 (Upstate Biotechnology, Lake Placid, NY) diluted 1:200, smooth muscle α actin diluted 1:100 (1A4, Dako, Carpinteria, CA) and macrophages (RAM-11; Dako) diluted 1:200. After washing three times, the sections were incubated for 45 minutes at room temperature with a goat anti-mouse IgG antibody conjugated with fluorescein isothiocyanate (Santa Cruz Biotechnology) using a spectral imaging fluorescence microscope system (OLYMPUS Optical Co., Ltd., Tokyo, Japan).

Separation of Unprocessed and Geranylgeranylated RhoA and Rac1

Unprocessed and geranylgeranylated forms of RhoA and Rac1 were separated by the Triton X-114 partition method as described previously[9]. The aortas were cut into small pieces and solubilized with a buffer containing 50 mmol/L Tris-HCl pH 7.5, 150 mmol/L NaCl, 5 mmol/L $MgCl_2$, 200 μmol/L GDP, 1 mmol/L dithiothreitol, 1 mmol/L pefabloc, 20 μmol/L

each of leupeptin, aprotinin and soybean trypsin inhibitor, and then sonicated. Triton X-114 (11% (w/v)) was added to the lysates to a final concentration of 1% (v/v). The lysates were mixed for 10 minutes at 4℃ and centrifuged at 15,000 g at 4℃ for 30 minutes to remove insoluble materials. The supernatant was warmed at 37℃ until it became cloudy, and then centrifuged at 400 g for 4 minutes at room temperature to separate the upper (unprocessed) phase from the lower (geranylgeranylated) phase. Both phases were adjusted to 1% (v/v) Triton X-114 on ice, and protein concentrations were determined by the Bradford method. The protein levels of RhoA and Rac1 were determined by Western blotting, followed by densitometric analysis. Briefly, aliquots containing 20 μg protein were subjected to electrophoresis, and the proteins were then transferred to polyvinylidene difluoride membranes. After incubating with blocking solution at room temperature for 30 minutes, the membranes were incubated for 60 minutes at room temperature with mouse monoclonal antibodies against RhoA diluted 1:250 and Rac1 diluted 1:500, followed by incubation with horseradish peroxidase-conjugated goat anti-mouse IgG (Santa Cruz Biotechnology). Signals from immunoreactive bands were visualized by fluorography with an Amersham ECL™ System (Amersham Pharmacia Biotech UK Ltd., Buckinghamshire, England).

Membrane Translocation of RhoA, Rac1 and $p47^{phox}$

The protein levels of RhoA and Rac1 in membrane fractions of the aortas were determined as described previously[8, 16]. For the preparation of membrane fractions of aortas, the isolated aortas were cut into small pieces, solubilized with a hypotonic buffer (10 mmol/L Tris, 2 mmol/L EDTA, 20 μg/mL antipain, 20 μg/mL leupeptin, 1 μmol/L DTT, and 1 μmol/L PMSF) and centrifuged at 15,000 g for 10 minutes at 4℃, followed by Western blotting.

GTP-loading of RhoA and Rac1

The levels of GTP-bound forms of RhoA and Rac1 of the aortas were determined by pull-down assays as described previously[8, 9, 18]. The removed aortas were cut into small pieces and lysed in a buffer (50 mmol/L Tris, pH 7.2, 500 mmol/L NaCl, 10 mmol/L $MgCl_2$, 1% Triton X-100, 0.5% sodium deoxycholate, 0.1% SDS, 20 μg/mL antipain, 20 μg/mL leupeptin, and 1 mmol/L PMSF). After centrifugation at 18,000 g at 4℃ for 10 minutes, the extracts were incubated for 45 minutes at 4℃ with glutathione-Sepharose 4B beads coupled with glutathione-S-transferase (GST)-rhotekin fusion protein for determination of RhoA activity and GST-p21-activated kinase (PAK) for Rac1 activity. Bound RhoA and Rac1 proteins were quantitated by Western blotting as described above.

The activity ratios of RhoA and Rac1 of the aortas at the ages of 3, 7 and 15 months were determined by dividing the levels of RhoA and Rac1 in the membrane fractions by the total cellular levels of RhoA and Rac1.

Preparation of Oxidized Low-Density Lipoproten (LDL)

Human LDL was isolated from sera of fasting normolipidemic volunteers by sequential ultracentrifugation, and oxidized LDL was prepared by incubating native LDL for 24 hours at 4℃ in phosphate-buffered saline (PBS) containing 5 μmol/L $CuSO_4$, and then extensively dialyzed against PBS and sterilized by filtration as described previously[19].

Densitometric Analysis

After scanning blots onto a computer (EPSON GT5500ART), individual bands were analyzed for optical density using NIH image as described previously[9, 20]. The area analyzed for each band was kept constant for each blot analyzed. Background density was subtracted from the densitometric data of each band.

Statistical Analysis

Statistical analyses were performed using ANOVA with Scheffé's post hoc test and Student's unpaired *t* test, as appropriate. A level of $p < 0.05$ was considered significant. Data are expressed as the means ± SD.

Results

Histological Analysis

Fig. 1A shows photomicrographs of the aortic atherosclerotic lesions in WHHLMI rabbits at 3, 7, 15 and 24 months by Azan-Mallory staining. Early atherosclerotic lesions were noted at 3 months with macrophage infiltration into the superficial portion. Smooth muscle cell infiltration and extracellular matrix deposit were already in progress. Lesion formation markedly progressed at the age of 7 months with abundant cellular infiltration of macrophages and smooth muscle cells (SMCs), and foam cell formation was prominent. Macrophages and foam cells were observed in the media. In contrast, atheromatous lesions at the ages of 15 and 24 months had decreased cellular components of macrophages and SMCs with increases in collagen fibers, extracellular lipid deposits,

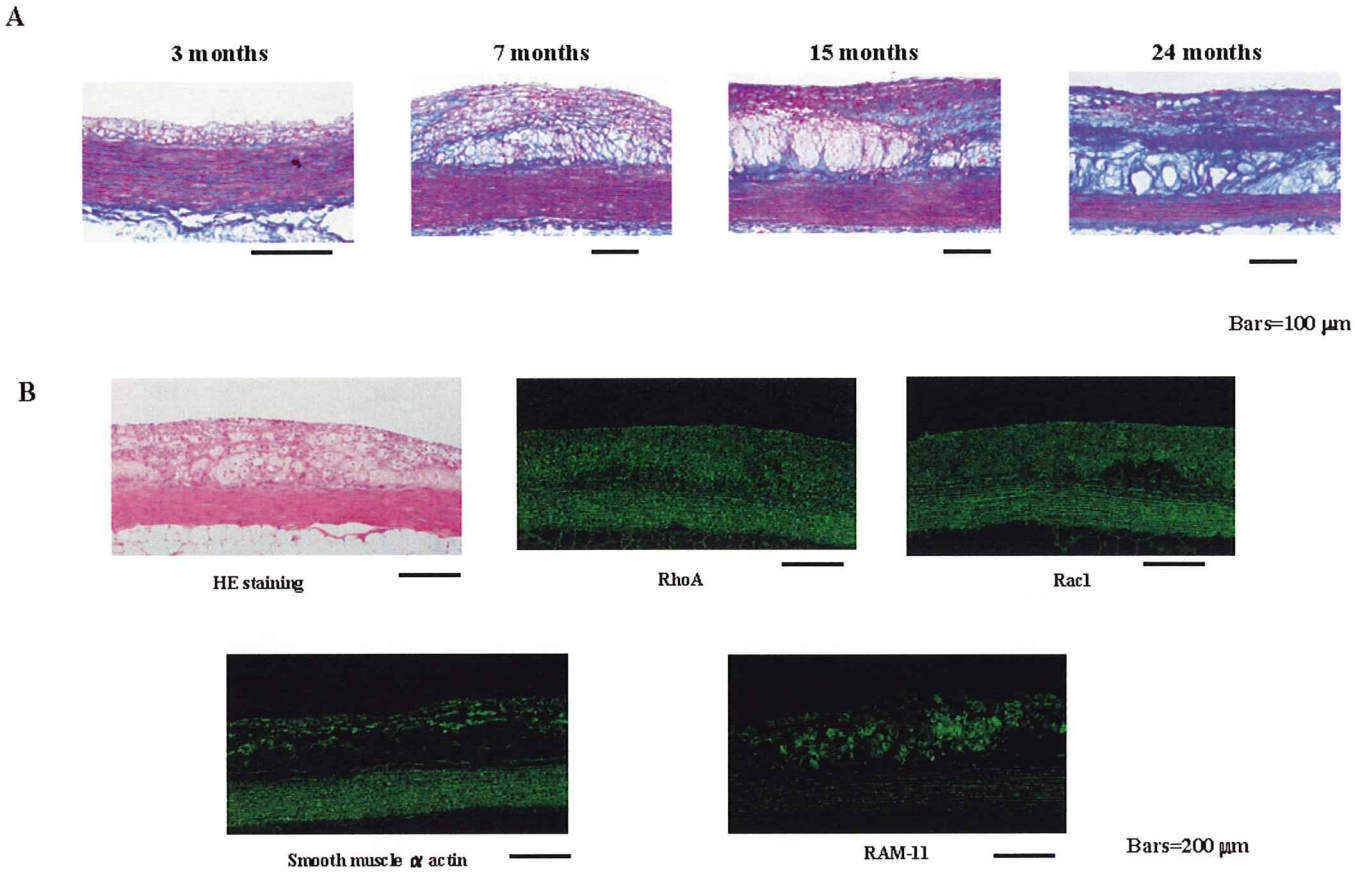

Fig. 1. A Representative photomicrographs showing aortic atherosclerotic lesions of WHHLMI rabbits with aging.

Thoracic aortas of the rabbits were removed at 3, 7, 15 and 24 months, and the sections were stained with Azan-Mallory staining. B Representative photomicrographs of fluorescent immnohistochemistry of RhoA, Rac1 smooth muscle α actin and macrophages (RAM-11) in atherosclerotic lesions of the aortas of WHHLMI rabbits at 7 months, as well as H&E staining.

cholesteryl crystals, and calcification.

RhoA and Rac1 in Aortic Atherosclerotic Lesions

Fluorescent immunohistochemistry of the atherosclerotic lesions at 7 months demonstrated that RhoA and Rac1 expression was noted in the atherosclerotic lesions and primarily colocalized with SMCs and macrophages (**Fig. 1B**).

Proportions of Unprocessed and Geranylgeranylated RhoA and Rac1 with Aging

We examined the proportions of the unprocessed and geranylgeranylated forms of RhoA and Rac1 in atherosclerotic lesions of the aortas at 3, 7, 15 and 24 months, as determined by the Triton X-114 partition method. The percentages of the unprocessed and geranylgeranylated forms of RhoA at 3 months were 25 ± 10% and 75 ± 10%, whereas at the age of 7 months the proportions of unprocessed RhoA had markedly increased to 75 ± 10% with decreased values of 25 ± 10% of geranylgeranylated RhoA (**Fig. 2A**, **2B**, $n=4$, $p<0.01$). At the ages of 15 and 24 months, the proportions of unprocessed and geranylgeranylated RhoA were similar to those at age of 7 months (15 months, 81 ± 6% and 19 ± 6%; and 24 months, 78 ± 7% and 22 ± 7%, $n=4$, $p<0.01$, each) as shown in **Fig. 2C**, **2D**.

Interestingly, the levels of unprocessed RhoA were markedly increased 6.6-, 4.6- and 2.5-fold with aging at 7, 15 and 24 months compared with at 3 months (**Fig. 2E**, $n=4$, $p<0.005$). In contrast, the proportions of geranylgeranylated RhoA at 7, 15 and 24 months were significantly decreased compared to at 3 months (**Fig. 2F**, $n=4$, $p<0.005$). The total amounts of RhoA increased with aging and peaked at 7 months (1.8-fold) compared with at 3 months (**Fig. 2G**, $n=4$, $p<0.05$), and a gradual decrease was noted with further aging after 7 months (**Fig. 2G**, 7 months vs. 24

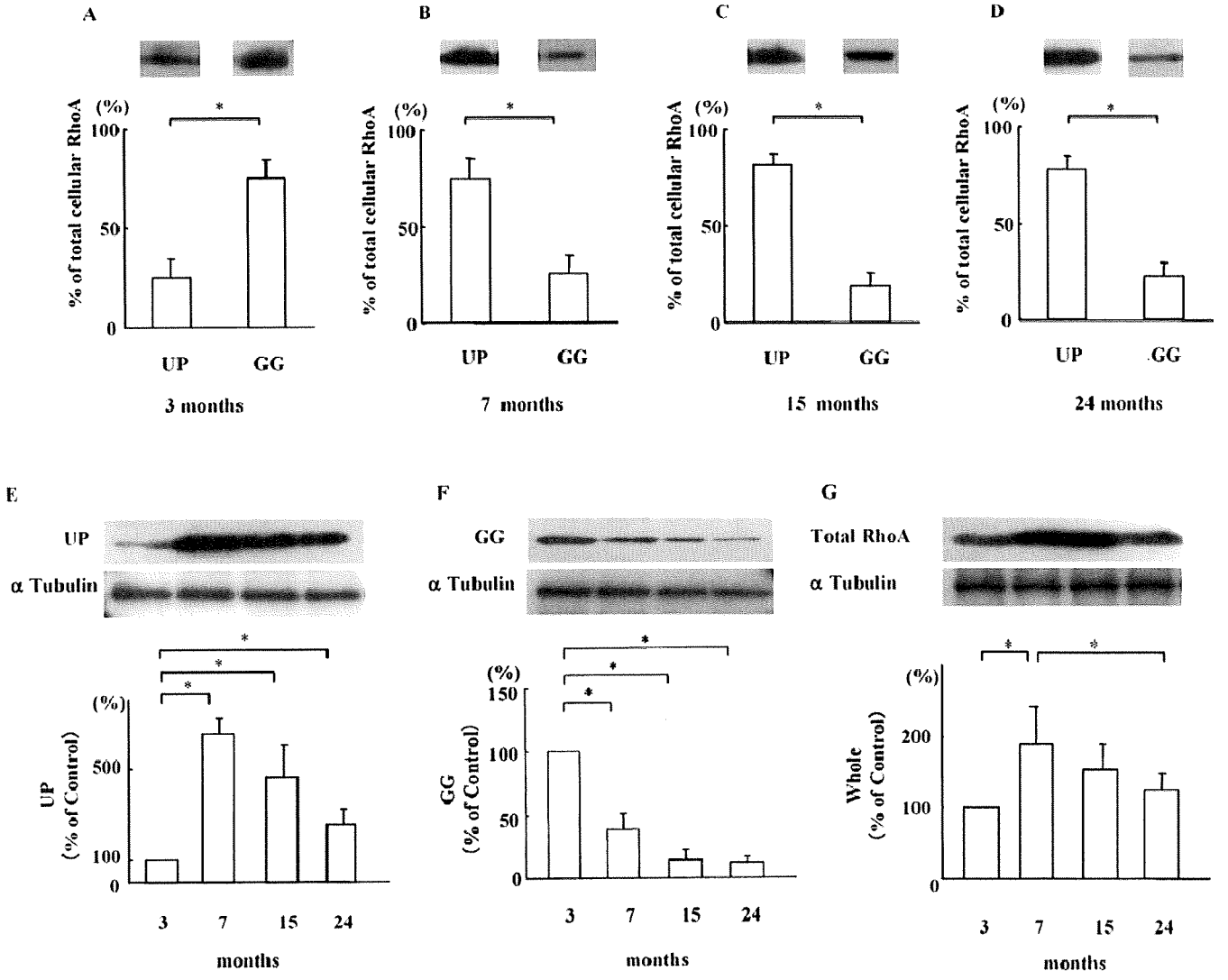

Fig. 2. A–D Percentages of unprocessed and geranylgeranylated forms of RhoA in atherosclerotic lesions of the aortas at 3, 7, 15 and 24 months, as determined by the Triton X-114 partition method.

The amounts of RhoA protein per 20 μg applied protein were determined by Western blotting. Representative immunoblots from four independent experiments are shown at the top. Values are the means ± SD of quantitative densitometric analyses. $^{*}p < 0.05$.

E–G, Changes in the proportions of unprocessed (E), geranylgeranylated and total (F) RhoA (G) in the aortas with aging (3, 7, 15 and 24 months).

The same filters were re-probed with an anti-α tubulin antibody for the normalization of cell lysates. Bars are the means ± SD of control values at 3 months from four separate experiments by quantitative densitometric analyses. Representative immunoblots of four independent experiments are shown at the top. UP indicates unprocessed GDP-RhoA and GG, geranylgeranylated RhoA. $^{*}p < 0.05$.

months, $n = 4$, $p < 0.05$).

The proportions of the unprocessed and geranylgeranylated forms of Rac1 changed with aging similar to RhoA, indicating that the percentages of unprocessed and geranylgeranylated Rac1 at 7, 15 and 24 months were reversed compared with those at 3 months (3 months, 26 ± 11% and 74 ± 11%; 7 months, 61 ± 6% and 39 ± 6%; 15 months, 74 ± 9% and 26 ± 9%; and 24 months, 72 ± 7% and 28 ± 7%, **Fig. 3A** to **3D**, $n = 4$, $p < 0.01$, each). The amounts of unprocessed Rac1 were increased 5.5-, 4.5- and 4.7-fold with aging at 7, 15 and 24 months compared with at 3 months and the percentages of geranylgeranylated Rac1 were significantly decreased after 7 months

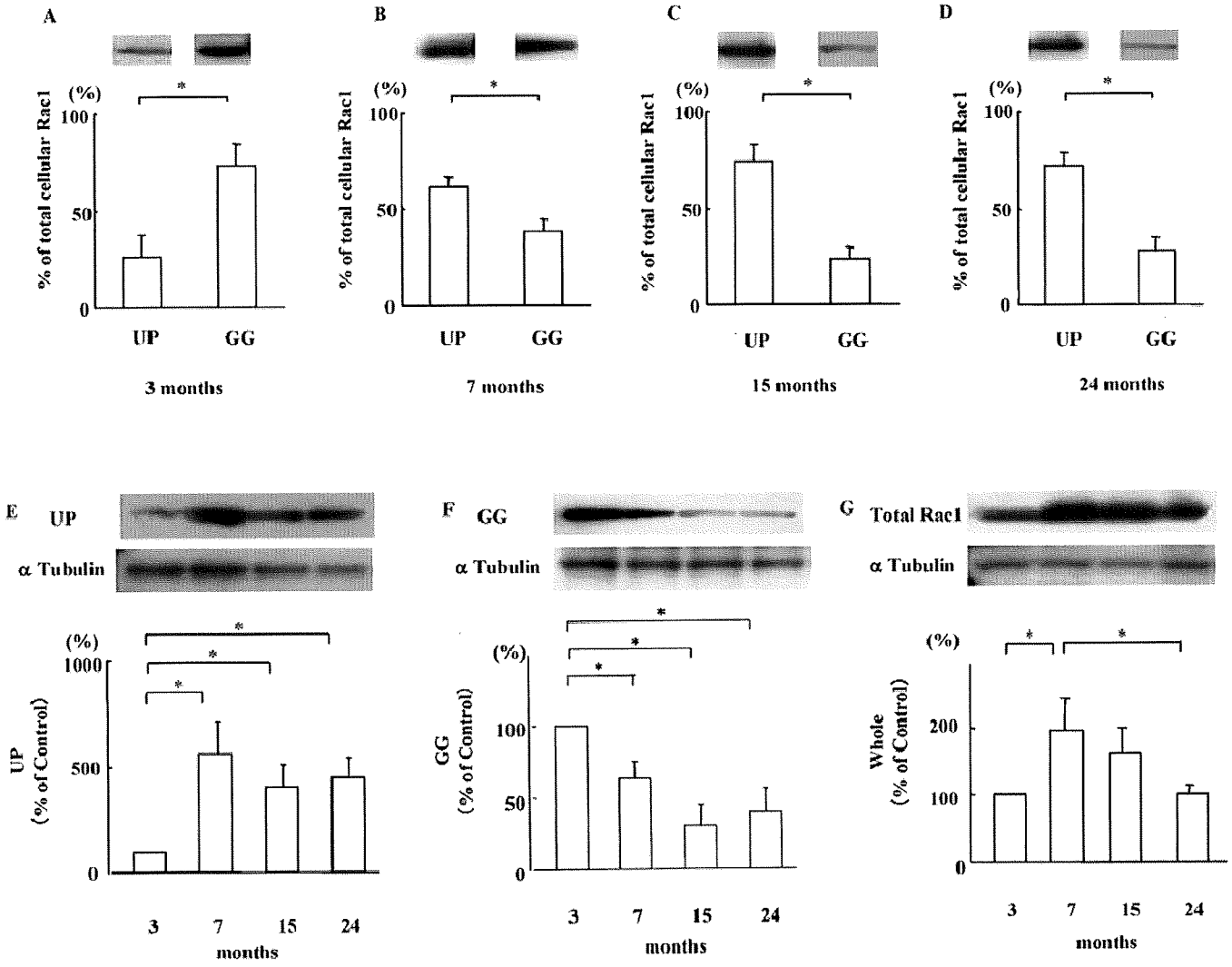

Fig. 3. Proportions of unprocessed and geranylgeranylated forms of Rac1 of the aortas at 3, 7, 15 and 24 months as described above.

A–D, Percentages of unprocessed and geranylgeranylated Rac1 of the atherosclerotic lesions of aortas at each time interval. Representative immunoblots from four independent experiments are shown. Values are the means ± SD of quantitative densitometric analyses from four separate experiments. $^{*}p<0.05$. E–G, Changes in proportions of unprocessed (E), geranylgeranylated (F) and total Rac1 (G) in aortas with aging (3, 7, 15 and 24 months). Representative immunoblots of four independent experiments are shown. Bars are the means ± SD of control values at 3 months from four separate experiments. $^{*}p<0.05$.

(**Fig. 3E, 3F**, $n=4$, $p<0.005$, each). The total amounts of Rac1 were increased with aging, similar to RhoA, with the peak value at 7 months (1.8 folds) compared with at 3 months (**Fig. 3G**).

Activities of RhoA and Rac1 with Aging in Atherosclerotic Lesions

Next, we examined the activities of RhoA and Rac1 in atherosclerotic lesions of WHHLMI rabbit aortas at the ages of 3, 7 and 15 months as determined by membrane translocation. The protein levels of RhoA and Rac1 in membrane fractions of the aortas at 7 months with advanced atherosclerotic lesions were markedly increased compared with at 3 months (**Fig. 4A, 4D**, $n=4$, $p<0.05$, each). At the age of 15 months the increased protein levels of membrane-bound RhoA and Rac1 had almost returned to the levels at 3 months (**Fig. 4A, 4D**, $n=4$, $p<0.05$, each). **Fig. 4B, 4E** show an increase in total RhoA and Rac1, respectively ($n=4$, $p<0.05$, each). These results represented the activity ratios of RhoA and Rac1 (**Fig. 4C, 4F**), indicating that the activities of RhoA and Rac1 at 7 months with accumulated atherosclerotic lesions were significantly enhanced compared with at 3

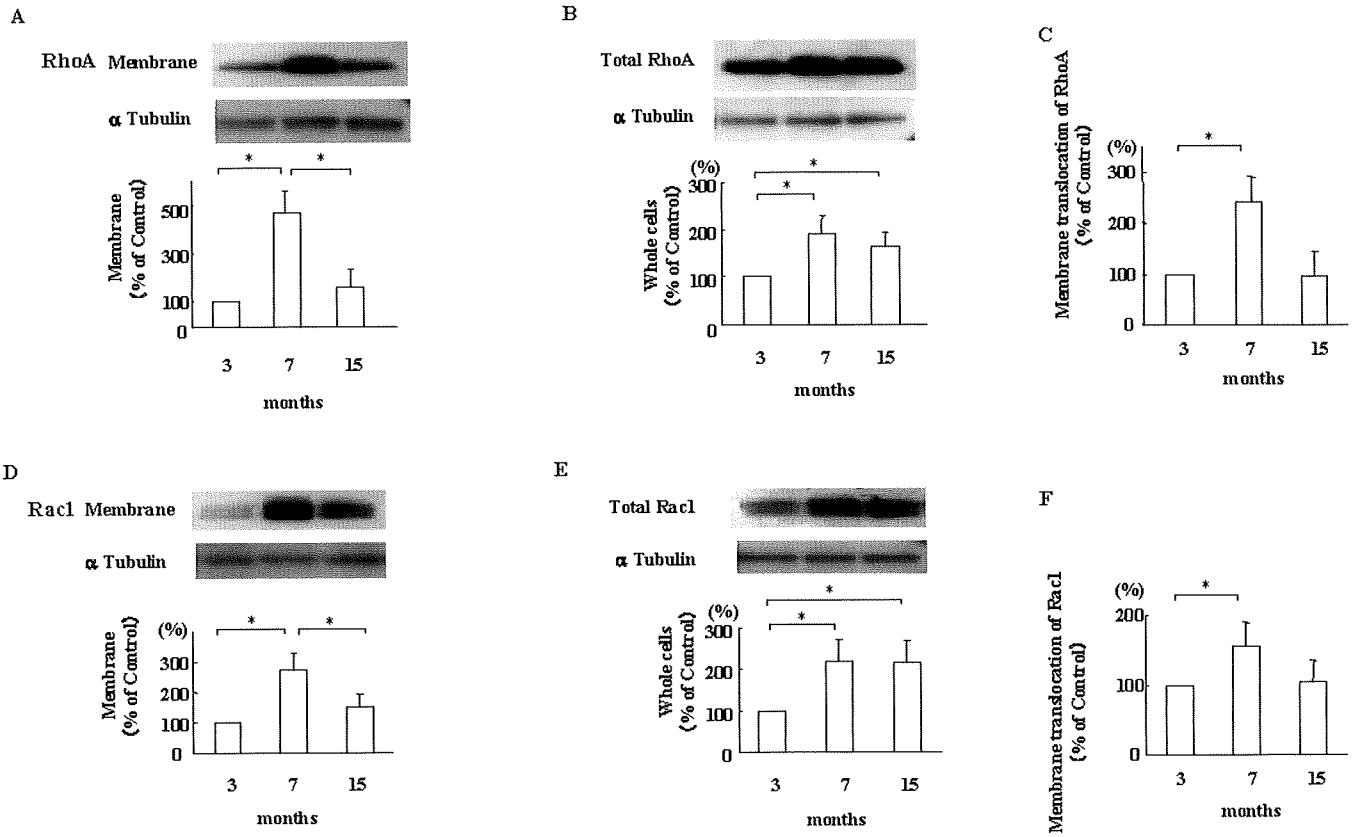

Fig. 4. Activities of RhoA and Rac1 in atherosclerotic aortas at ages 3, 7 and 15 months were determined by membrane translocation.

A and D, Levels of RhoA (A) and Rac1 (D) in the membrane fractions were determined. Results represent the means ± SD of four separate experiments of quantitative densitometric analysis, and immunoblots are from representative experiment $^{*}p<0.05$. B and E, Levels of total RhoA (B) and Rac1 (E) in the aortas. Results represent the means ± SD of four separate experiments and immunoblots from representative experiment $^{*}p<0.05$. C and F, Activity ratios of RhoA (C) and Rac1 (F) of the aortas at ages of 3, 7 and 15 months were determined by dividing the levels of RhoA and Rac1 in membrane fractions by the total cellular levels of RhoA and Rac1, respectively. Results represent the means ± SD of four separate experiments $^{*}p<0.05$.

months with early atherosclerotic lesions ($p<0.05$, each).

To determine indirectly the activity of guanine nucleotide exchanging factor (GEF) responsible for GDP/GTP exchange of RhoA and Rac1, we performed pull-down assays using aortas at the ages of 3 and 7 months. **Fig. 5A, 5B** show that the GTP-loading of RhoA and Rac1 of the aortas at the 7 months were significantly increased compared with at 3 months ($n=6$, $p<0.005$, each). Moreover, the activity of $p47^{phox}$ was determined by membrane translocation, indicating that the activity of $p47^{phox}$ of the aortas at 7 months was significantly increased approximately 2-fold compared with at 3 months ($n=4$, $p<0.05$, data not shown).

Effect of Oxidized LDL on Total Protein Levels of RhoA and Rac1 in Cultured SMCs

Finally, to clarify the influence of hyperlipidemia on RhoA and Rac1 metabolism *in vitro*, we examined the effect of oxidized LDL on the protein levels of RhoA and Rac1 in cultured rabbit SMCs. Incubation with oxidized LDL tended to increase the protein levels of RhoA and Rac1 in SMCs. **Fig. 6** shows a significant increase in the protein levels of RhoA and Rac1 in SMCs stimulated with 25 μg/mL oxidized LDL after 48 hours of incubation, but not 24 hours.

Discussion

The present study shows for the first time the profile of unprocessed and geranylgeranylated forms of RhoA and Rac1 with aging in the atherosclerotic

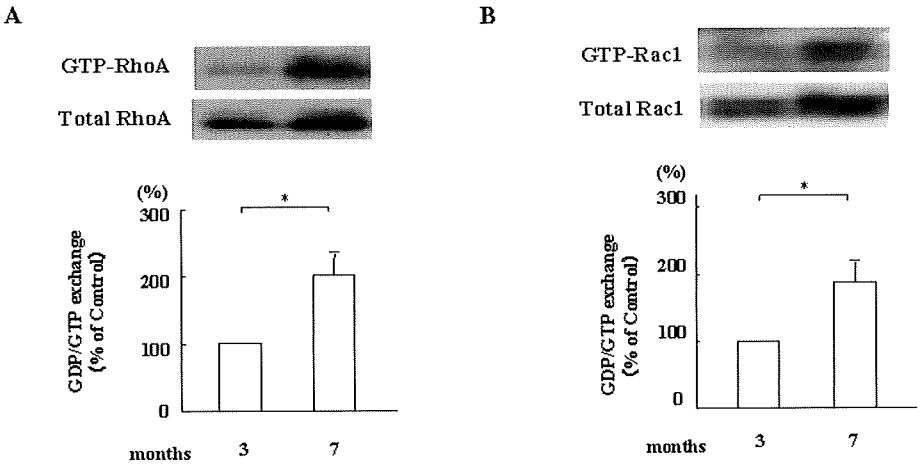

Fig. 5. GTP-loading of RhoA (A) and Rac1 (B) of aortic atherosclerotic lesions at 3 and 7 months.

Levels of GTP-bound active forms of RhoA and Rac1, which were normalized by the total levels of RhoA and Rac1. GTP-RhoA indicates the GTP-bound active form of RhoA and GTP-Rac1, the GTP-bound active form of Rac1. Representative immunoblots are shown at the top. Bars are the means ± SD of quantitative densitometric analyses from six separate experiments $^{*}p<0.005$.

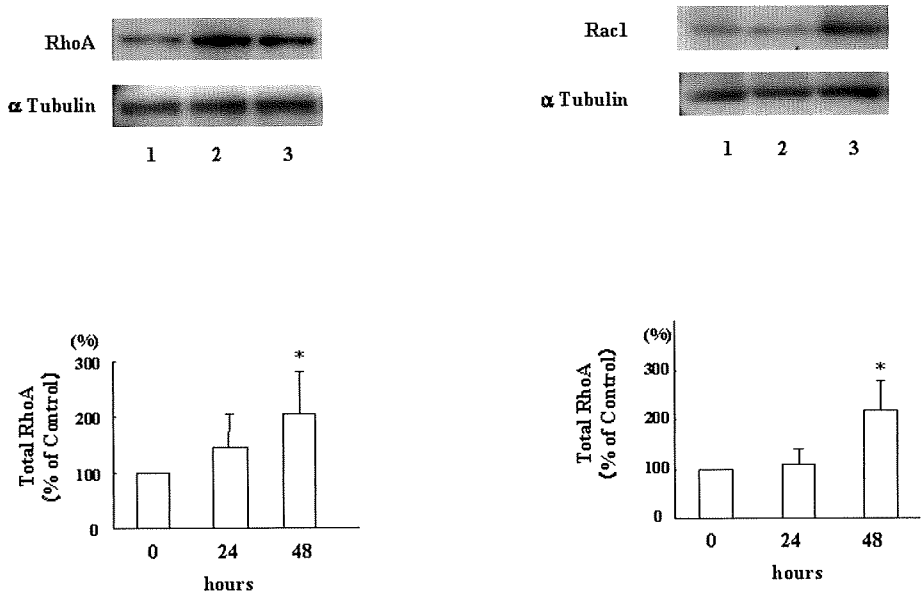

Fig. 6. Effect of oxidized LDL on the protein levels of total RhoA and Rac1 in cultured rabbit SMCs.

SMCs were cultured in the presence of 25 μg/mL oxidized LDL for up to 48 hours, followed by Western blotting. Bars are the means ± SD of three similar experiments. Representative immunoblots are shown $^{*}p<0.05$.

lesions of a novel atherosclerosis animal model of WHHLMI rabbits, indicating that the amounts of unprocessed RhoA and Rac1 increased with cellular infiltration in the progression of atherosclerosis. Data also showed that the activities of RhoA and Rac1 were enhanced in atherosclerotic lesions with cellular infiltration at 7 months compared with early atherosclerotic lesions at 3 months. These findings suggest that the potency of the increased pool of unprocessed RhoA and Rac1 may play a role in the pathogenesis of